Machine Learning for High-Entropy Alloys

Shuai Chen, Yuan Cheng, and Huajian Gao

1 Overview of High-Entropy Alloys

In 2004, Yeh et al. [1] and Cantor et al. [2] independently proposed a novel category of multi-principal component alloys consisting of five or more constituent elements with atomic compositions between 5 and 35 atomic percent, which are today widely termed as HEAs. With multi-principal components, HEAs possess unique microstructures with fundamental core effects and exhibit many impressive properties for practical applications. In this section, we will give an overview of HEAs. Four fundamental core effects of HEAs are discussed in Sect. 1.1. Some popular preparation methods of HEAs are introduced in Sect. 1.2. The reported excellent properties of HEAs are summarized in Sect. 1.3.

S. Chen
Institute of High Performance Computing, A*STAR, Singapore, Singapore
e-mail: chens@ihpc.a-star.edu.sg

Y. Cheng (✉)
Monash Suzhou Research Institute, Suzhou, P.R. China
e-mail: Yuan.Cheng@monash.edu

H. Gao
Institute of High Performance Computing, A*STAR, Singapore, Singapore

School of Mechanical and Aerospace Engineering, College of Engineering, Nanyang Technological University, Singapore, Singapore
e-mail: huajian.gao@ntu.edu.sg

Y. Cheng et al. (eds.), *Artificial Intelligence for Materials Science*, Springer Series in Materials Science 312, https://doi.org/10.1007/978-3-030-68310-8_2

1.1 Fundamentals of High-Entropy Alloys

Due to the complex elemental compositions, the outstanding mechanical properties of HEAs are featured by four fundamental core effects, which are summarized as: (1) high-entropy effect for thermodynamics; (2) sluggish diffusion effect for kinetics; (3) severe lattice distortion effect for structures; and (4) cocktail effect for properties. High-entropy effect determines the thermodynamic equilibrium phase and associated microstructure. Sluggish diffusion effect influences the kinetics during phase transformation. Severe lattice distortion effect affects the deformation behaviour and the structure-property relation. Cocktail effect implies the unexpected behaviour appeared after alloying different elements. We will discuss these four fundamental core effects separately.

1.1.1 High-Entropy Effect

It was first proposed by Yeh et al. [1] that, in multi-principal component alloys consisting of five or more elements in near equimolar concentrations, intermetallic compounds could be suppressed and solid-solution phases stabilized by the high-entropy effect. Based on the second law of thermodynamics, at given pressure and temperature, an alloy system attains its thermodynamically equilibrium state if its Gibbs free energy is the lowest [3]. The Gibbs free energy of forming alloys from mixing elemental components is expressed as:

$$\Delta G_{\text{mix}} = \Delta H_{\text{mix}} - T\Delta S_{\text{mix}} \tag{1}$$

where ΔG_{mix} is the Gibbs free energy of mixing, ΔH_{mix} the enthalpy of mixing, T the absolute temperature, and ΔS_{mix} the entropy of mixing.

The entropy of mixing can be calculated from the following four contributions:

$$\Delta S_{\text{mix}} = \Delta S_{\text{mix}}^{\text{conf}} + \Delta S_{\text{mix}}^{\text{vib}} + \Delta S_{\text{mix}}^{\text{elec}} + \Delta S_{\text{mix}}^{\text{mag}} \tag{2}$$

where $\Delta S_{\text{mix}}^{\text{conf}}$ is the configurational entropy, $\Delta S_{\text{mix}}^{\text{vib}}$ the vibrational entropy, $\Delta S_{\text{mix}}^{\text{elec}}$ the electronic randomness entropy, and $\Delta S_{\text{mix}}^{\text{mag}}$ the magnetic dipole entropy. The configurational entropy is always dominant among all four types of entropies, and represents the mixing entropy in the alloys system [3]. For an alloy system of n elements in a random solid solution, the configurational entropy is [4]:

$$\Delta S_{\text{mix}}^{\text{conf}} = -R\sum_{i=1}^{n} c_i \ln c_i \tag{3}$$

where R is the gas constant, and c_i is the mole fraction of the i^{th} element. The enthalpy of mixing for the n-element alloy can be calculated as [5]:

$$\Delta H_{\text{mix}} = \sum_{i=1, i\neq j}^{n} 4\Delta H_{\text{AB}}^{\text{mix}} c_i c_j \tag{4}$$

where ΔH_{AB}^{mix} is the mixing enthalpy of binary equimolar AB alloys, and the values can be obtained from literature [5, 6].

Elemental phases with one principal element have slightly negative ΔH_{mix} and slightly positive ΔS_{mix}, intermetallic compounds possess highly negative ΔH_{mix} but slightly positive ΔS_{mix}, and solid-solution phases consisting of multiple elements feature moderately negative ΔH_{mix} but highly positive ΔS_{mix}, which enhances their stability. Therefore, high-entropy effect helps to stabilize the formation of solid-solution phases with superior properties.

1.1.2 Sluggish Diffusion Effect

The diffusion is sluggish in HEA, as compared with conventional alloys. Diffusion is difficult to measure experimentally, so early support of this effect relies on indirect evidence [4], such as secondary observations that include formations of nanocrystals and amorphous phases upon solidification and on qualitative interpretations of microstructural stability upon cooling. Direct diffusion experiments were performed by Tsai et al. [7] in 2013 with a near-ideal solution system of CoCrFeMnNi in stable single face-centre-cubic (FCC) solid solution. The experimental measurements showed that the diffusion coefficients in the CoCrFeMnNi HEA are lower than those in the FCC FeCrNi alloys and FCC pure metals. Correspondingly, the activation energies in the HEA are higher than those in the FeCrNi alloys and pure metals. Among the five elements in the CoCrFeMnNi HEA, Ni is the slowest diffusing element, while Mn is the fastest diffusing element. The order of increasing diffusion rate is Ni < Co < Fe < Cr < Mn. Because of the diversity of atoms surrounding each lattice site, an atom/vacancy can face a variable path to diffuse/migrate, and the vacancy trapping effect of low-energy sites would lead to the sluggish diffusion.

To evaluate the quantity of low-energy sites and high-energy barriers, the energetic data for the vacancy migration in the CoCrFeMnNi HEA have been quantitatively examined based on atomistic simulations [8]. Initially, a vacancy on a lattice site (numbered "0" in Fig. 1a) was introduced in a sample from the Canonical Monte Carlo (CMC) simulation. Then, a nearest neighbouring atom was moved to the vacant site. After each movement, the neighbouring atoms surrounding the vacancy were relaxed. Finally, the variation of potential energy with positions as the atoms repeatedly move is plotted in Fig. 1b. Because the migration of a vacancy to a nearest neighbouring site corresponds to the opposite movement of the neighbouring atom, the energy barrier of vacancy migration could be calculated according to the potential energy curve. The average energy barriers for the five elements are shown in Fig. 1c. These data demonstrate that the average migration energy barriers are different for the five elements, and the order is Ni > Co > Cr > Fe > Mn, which is close to the diffusivity measured in experiment (Ni < Co < Fe < Cr < Mn) [7].

Sluggish diffusion effect is very important for HEA since it provides many advantages [3]. For example, sluggish diffusion facilitates super-saturated states and fine precipitates in HEA structures. It can also enhance the creep resistance,

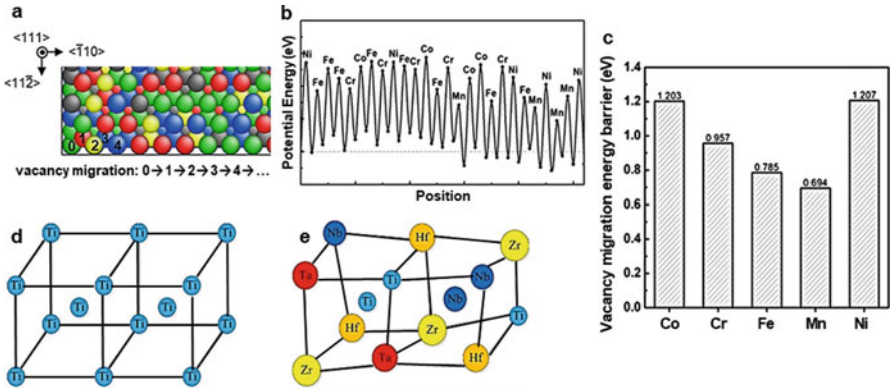

Fig. 1 (**a**) A schematic diagram of an HEA sample with a vacancy. (**b**) Variation of potential energy with vacancy position during the vacancy migration. (**c**) Average energy barrier of vacancy migration for the five elements [8]. A schematic illustration of BCC crystal structure: (**d**) perfect lattice of β-Ti metal; (**e**) severely distorted lattice of TiNbTaZrHf HEA [9]

weaken the particle coarsening, increase the recrystallization temperature, and reduce the grain growth rate, which benefit the microstructures and properties of HEAs for high-performance structural materials. Moreover, in practical applications demanding slow diffusion kinetics, such as high-temperature applications, this effect makes HEAs extremely competitive.

1.1.3 Severe Lattice Distortion Effect

A solid-solution phase is formed stably as a whole matrix in a HEA due to high-entropy effect, regardless of the fact whether its structure is body-centre-cubic (BCC), FCC, hexagonal-close-packed (HCP), B2 (ordered BCC), or $L1_2$ (ordered FCC). In the matrix, there is severe lattice distortion since every atom in the lattice site is surrounded by diverse types of atoms. As shown in Fig. 1d [9], the pure β-Ti metal has a perfect BCC crystal structure, which consists of atoms with the same size. Adding Nb, Ta, Zr, and Hf elements in the β-Ti metal for composing TiNbTaZrHf HEA, as shown in Fig. 1e, results in severe lattice distortions due to different sized atoms, where the elemental components are considered to occupy a lattice site with the same probability. Due to the severe lattice distortions, the crystal structure of HEA suffers local lattice strain and stress, making dislocation motion more difficult, as compared with the pure metals or conventional alloys.

A quantitative parameter considering the atomic size difference by Zhang et al. [5] is widely used to evaluate the lattice distortion.

$$\delta = \sqrt{\sum_{i=1}^{n} c_i (1 - r_i/\overline{r})^2} \tag{5}$$

where n is the number of elemental components in the HEA system, c_i the mole fraction of the i^{th} element, r_i the atomic radius of the i^{th} element, and $\overline{r}$ the average atomic radius $\left(= \sum_{i=1}^{n} c_i r_i \right)$.

Direct characterizations of lattice distortion are extremely challenging in experiment. The pair distribution function (PDF), which describes the distribution of distances between atomic pairs contained within a given volume, has been utilized to quantitatively estimate the distorted local structure of HEA by Tong et al. [10] under the measurement of high-energy synchrotron X-ray and neutron scattering. Based on the PDF measurement, the lattice distortion can be quantified as $\varepsilon = (a_{1\text{st}} - a_{\text{avg}})/a_{\text{avg}}$, where $a_{1\text{st}}$ is the lattice parameter obtained by fitting to the first peak of PDF curve, and a_{avg} is the lattice parameter obtained by fitting to the overall spectrum. Tong et al. [10] found that the FeCoNiCrPd HEA had a lattice distortion parameter $\varepsilon = 0.79\%$, about twice as large as that of the $Ni_{80}Pd_{20}$ alloy ($\varepsilon = 0.41\%$). Clearly, substituting Ni atoms with similar-sized Fe, Co, and Cr atoms resulted in a dramatic increase in lattice distortion. This unexpected increase cannot be simply explained by the difference in atomic size. Besides the atomic size difference, differences in crystal-structure tendencies (FCC, BCC, HCP, B2, or $L1_2$) and bonding energies among constituents can also cause severe lattice distortions. The lattice distortion effect is very broad, which not only influences the thermodynamic stability and deformation mechanisms, but can also affect a wide range of other properties. For example, the lattice distortion seems to have some effect on ductility and can substantially improve the friction stress, leading to enhanced strength and sensitivity to the grain size [11, 12].

1.1.4 Cocktail Effect

The cocktail effect is a term commonly used in the acoustic field to describe the ability to focus one's listening attention on the voice of a single speaker among a mixture of other conversations and background noises [13]. Multi-metallic cocktail effect was first put forward by Ranganathan [14] to highlight the advantages of conventional alloys, compared to which this effect becomes even more pronounced in HEAs. For HEAs, the cocktail effect refers to unexpected properties which do not exist in a single element but can be obtained by mixing diverse types of elements. This effect emphasizes the fact that the properties of HEA can be dramatically tuned by adjusting the elemental compositions and preparation method. Some examples on the excellent properties of HEAs due to the cocktail effect will be discussed in Sect. 1.3.

For an HEA, its crystal structure is a multicomponent solid solution, which can be considered as an atomic-scale composite. Therefore, its properties originate not

only from the intrinsic properties of the constituents following the mixture rules but also from the cocktail effects of mixing different elements, providing greater opportunities for alloy designers to achieve unprecedented properties. However, it is also challenging since the cocktail effect is complicated and difficult to predict based on the available theoretical frameworks. For example, the phase diagrams of most binary and ternary alloy systems are available. For HEAs, however, there is not a single integrated phase diagram to guide the researchers to design the alloys with specific target. Here, ML approach has proven useful in guiding the HEA design based on limited data. These four core effects play fundamental roles in the investigation and understanding on the microstructures and properties of HEAs. It can be expected that great efforts will be made to establish the fundamental framework of multi-principal HEAs in the coming years.

1.2 Preparation Methods of High-Entropy Alloys

The development of HEAs is closely associated with the investigation of amorphous alloys [13]. Therefore, the preparation and fabrication methods of HEAs often refer to those of amorphous alloys, which can be categorized into three major approaches [3]. The first approach is liquid-state mixing, which is also the main route, including arc melting, laser melting, inductive melting, electric-resistance melting, laser engineered net shaping, and laser cladding [15]. The second approach is solid-state mixing, containing mechanical alloying and subsequent consolidation. The third approach is gas-state mixing, and the techniques include sputter deposition, atomic layer deposition, pulse-laser deposition, molecular-beam epitaxy, and vapour-phase deposition. Through these preparation methods various morphologies of HEAs could be fabricated, including three-dimensional bulk, two-dimensional film/coating, and one-dimensional fibrous HEAs. We will choose one typical preparation method from each route for detailed introduction, i.e., arc melting, mechanical alloying, and sputter deposition.

1.2.1 Arc Melting

Arc melting is the dominant preparation method to synthesize bulk HEAs among the diverse fabrication routes. Figure 2a demonstrates a schematic diagram of the arc-melting method [16]. The temperature of torch can reach as high as 3000 °C, which is tuned by adjusting the electrical power. The arc-melting method is applicable to most of the elemental compositions, including those with high melting temperatures, by mixing them in the liquid state. However, this method may not be the best choice for those elements with a relatively low melting temperature, e.g., Mg, Mn, and Zn, since they tend to evaporate after heating. In that case, the elemental compositions of HEAs are difficult to be precisely controlled for arc melting if these elements are added. For these elements, electric-resistance melting or inductive melting may be much more suitable.

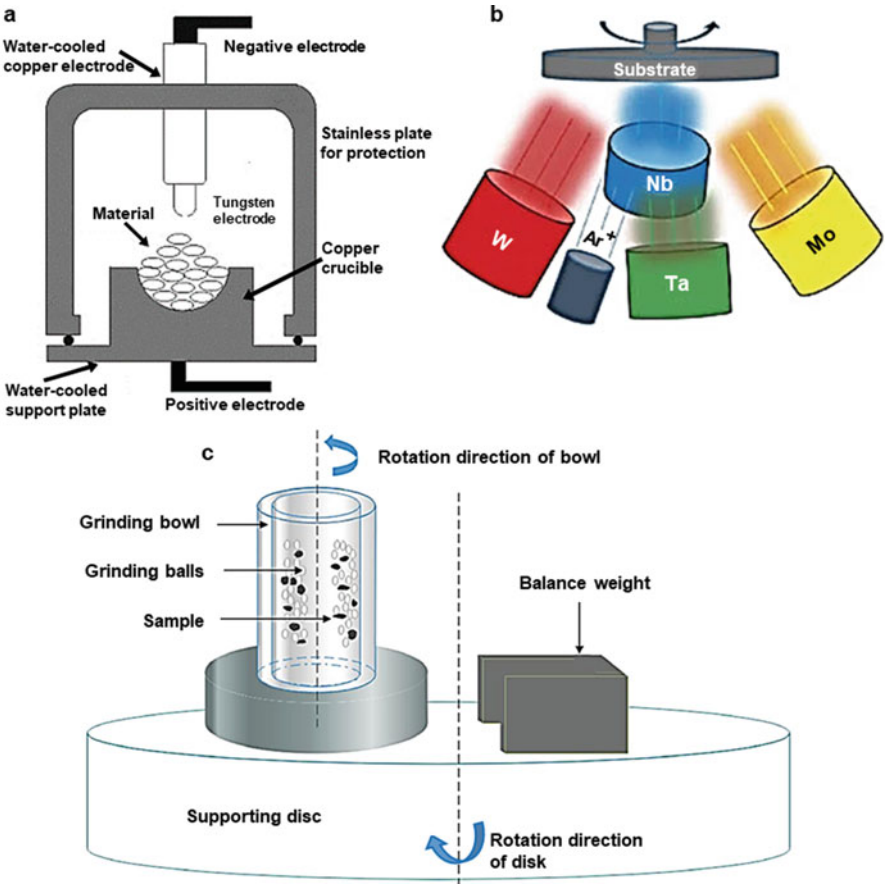

Fig. 2 A schematic diagram of HEA preparation methods: (**a**) arc melting [16]; (**b**) sputter deposition [17]; and (**c**) mechanical alloying [18]

Tsao et al. [16] synthesized an $Al_{0.3}CrFe_{1.5}MnNi_{0.5}$ HEA by the arc-melting method, as shown in Fig. 2a. The HEA sample was melted at a temperature around 1530–1580 °C for 2–3 min repeatedly and solidified with turning of the solidified ingots for five times to reach a completely alloyed state. The HEA microstructures consisted of dendrites (DR) as matrix and interdendrites (IR). IR were Ni-rich FCC phase, DR were Cr-rich BCC phase, and a small portion of cross-like Ni-rich FCC phase was also formed. The as-prepared samples were under heat treatment at 650–750 °C for 8 h and then quenched in water to further explore the effects of age treatment on the microstructure and hardness of this $Al_{0.3}CrFe_{1.5}MnNi_{0.5}$ HEA. After ageing at 650 °C, both AlNi and $Cr_5Fe_6Mn_8$ precipitations appeared within the DR, where cross-like FCC phase disappeared. During ageing at 750 °C, the AlNi precipitations in the DR were larger and formed globular shape inside the grain matrix, contributing to a hardening effect. This work demonstrates that dual-phase

(FCC + BCC) structures are formed in HEAs, and the precipitations are beneficial to the mechanical properties.

For the effect of cooling rate on the crystal structure and chemical composition of HEAs during arc melting, Singh et al. [19] performed a detailed investigation of AlCoCrCuFeNi HEA by melting the constituent elements in an induction levitation furnace and then following two different processing conditions (splat quenching and normal casting) in a copper crucible under a pure argon atmosphere. Normal casting was produced in flowing argon, which provided a normal cooling rate of 10–20 K/s. They observed similar microstructures consisting of dendrites and interdendrites in HEA samples after normal cooling as in Tsao et al.'s experiments [16]. Splat quenching was operated in vacuum (10^{-6} mbar) in an electromagnetic levitation chamber, which reached an ultrafast cooling rate of 10^6–10^7 K/s. Interestingly, a single BCC phase is obtained by ultrafast cooling. Singh et al.'s work [19] indicates that, for some HEAs, a solid-solution phase can only be formed at a relatively fast cooling rate, which is a metastable state. A relatively slow cooling rate causes the formation of multiple phases, leading to a remarkable reduction in the mixing entropy because of the elemental segregation among these phases [13].

1.2.2 Mechanical Alloying

Mechanical alloying is a processing technique of solid-state powder involving repeated cold welding, fracturing, and re-welding of powder particles in a high-energy ball mill [20]. A schematic diagram of mechanical-alloying method is shown in Fig. 2c [18]. Originally developed to produce oxide-dispersion strengthened Fe- and Ni-base superalloys for aerospace applications, mechanical alloying has been shown capable of synthesizing a wide variety of equilibrium and non-equilibrium alloys ranging from blended elemental to pre-alloyed powders. Mechanical alloying of HEAs normally follows a three-step procedure. First, the elemental constituents are mixed and milled into fine powders in a ball mill. Then, a hot-isostatic-pressing process is performed to impact and sinter these fine powders simultaneously. Last, a heat-treatment process is applied to remove internal stresses induced by cold compaction.

The greatest advantage of mechanical alloying is to synthesize novel HEAs that are impossible to prepare by other techniques, such as alloying of normally immiscible elements or directly coating HEA on a substrate. The reason is that the limitations imposed by phase diagrams are not applicable to mechanical alloying for its completely solid-state processing. The CrMnFeCoNi HEA is one of the most notable and promising HEAs that has been studied and widely termed as Cantor alloy. However, there are only a few published papers on CrMnFeCoNi HEA coating. Tian et al. [18] synthesized CrMnFeCoNi HEA coating on a Q235 steel substrate by mechanical-alloying method. First, HEA powders were prepared. Then, the Q235 substrate was put into the prepared powders. Last, a milling process was performed for 10 h, after that the HEA coating was successfully prepared. Both the as-prepared powders and the final coating presented single FCC solid solutions.

The coating thickness was 180 μm, exhibiting a good bonding strength with the substrate. The constituents were homogeneously distributed in the coating without component segregation. The corrosion results show that the HEA coated Q235 has better corrosion resistance than the pure Q235 in 3.5 wt% NaCl solution.

High-pressure torsion is a popular technique that achieves not only grain refinement up to the nanometre scale but also diverse phase transformations. Kilmametov et al. [21] applied the high-pressure torsion technique to a multicomponent powder for the first time to produce a bulk nanostructured CoCrFeMnNi HEA by high-pressure-torsion induced mechanical alloying. Micrometre sized elemental powders were blended in equimolar concentrations, consolidated and deformed at 5 GPa using imposed shear strain equivalent up to 100 rotations, leading to a fully dense bulk CoCrFeMnNi HEA. Single-phase nanocrystalline HEA (grain size of 50 nm) with smaller chromium oxide precipitates (particle size of 7–10 nm) exhibited an amazing hardness of 6.7 GPa, which is one of the highest reported values for bulk CoCrFeMnNi HEAs.

1.2.3 Sputter Deposition

Among gas-state preparation methods, sputter deposition, as shown in Fig. 2b [17], is the most widely used one to synthesize HEA films. To date, bulk HEAs have been extensively investigated, but small-dimensional HEAs have drawn less attentions, such as HEA films/coatings and small-sized pillars. With incremental demands for micro-/nanoscale devices for practical applications in high-temperature and harsh environments, the fabrication and investigation of small-dimensional HEAs become increasingly important, where magnetron-sputtering deposition exhibits great potentials. In the sputter deposition of HEAs, the sputtered atoms are ejected from the sputtering target by ion or atom bombardment from the sputtering gas, and then randomly deposited on the substrate to form HEA. The microstructures of the HEA are mainly determined by the processing parameters, including the form of source material, atmosphere pressure, work piece temperature, and substrate bias voltage.

Using magnetron co-sputtering technique, Zou et al. [17] deposited NbMoTaW HEA films and small-sized pillars on silicon and sapphire substrates at room temperature. Ion beam-assisted deposition (IBAD) method [22] was employed to reduce deposition rate and grain size. During mechanical testing under a nanoindenter, the HEA pillars exhibited extraordinarily high yield strengths of ~10 GPa, which were among the highest reported values for the compressions of micro- and nano-pillars. The strength of such HEA pillar was one order of magnitude higher than that of its bulk form, along with significantly enhanced ductility (compressive plastic strains > 30%). The HEA films demonstrated substantially enhanced stability under long-duration high-temperature conditions (at 1100 °C for 3 days). Such excellent properties of small-dimensional HEAs have potential applications in high-temperature and high-stress conditions.

1.3 Excellent Properties of High-Entropy Alloys

Since they were proposed in 2004, HEAs with extraordinary mechanical, physical, and chemical properties have been reported in succession, such as high hardness, enhanced strength–ductility synergy, excellent thermal stability, superior wear/corrosion/irradiation resistance, and high-performance catalytic properties [23–25]. Alloying-element compositions, crystal-phase structures, grain sizes, preparation techniques, and annealing treatments play important roles in the microstructural evolutions and associated properties of HEAs. Here we mainly discuss the hardness, strength–ductility synergy, and high-temperature properties of HEAs.

1.3.1 Hardness

Hardness is one of the most popular approaches to examining the mechanical properties of HEAs since Vickers hardness measurement can be performed efficiently and effectively with less requirement for the size and shape of the sample. For some thin films of HEAs, their yield stresses are difficult to measure directly, but micro-hardness tests can be easily performed with high precision. The hardness values of HEAs change widely in each alloy system. In the Al_xCoCrCuFeNi HEAs, the hardness varies from 133 to 655 HV when the x value increases from 0.0 to 3.0, along with a phase transformation from FCC to BCC structures [1]. With the substitution of Co or Cu with Mo or Ti, the hardness value generally increases. For example, $AlCo_{0.5}CrFeMo_{0.5}Ni$ and $Al_{0.2}Co_{1.5}CrFeNi_{1.5}Ti$ HEAs exhibit a high hardness value of 788 HV [26] and 717 HV [27], respectively. Thus, the selection of the HEA system and adjustment of the elemental concentrations are critical in determining the hardness of HEA.

To systematically investigate the compositional dependence of HEA hardness, Zhu et al. [28] tuned the atomic ratio of the constituent elements in three typical equimolar CoCrFeNiMn, CoCrFeNiAl, and CoCrFeNiCu HEAs to form 78 alloys, whose phase structures and hardness values are shown in Fig. 3. Single phase (FCC or BCC), duplex FCC phases, and duplex BCC phases, formed within a wide compositional space in 68 out of the 78 HEAs, were not limited to the equimolar compositions with the maximum mixing entropy. With the precipitation of hard sigma phases, the hardness of the FeNiCrMn alloy is 528 ± 82 HV (Fig. 3a). With Ni addition, the hardness decreases to 145–166 HV when x reaches 10% for $(CoCrFeMn)_{(100-x)}Ni_x$ HEAs due to the decreased volume fraction of sigma phase. $(CrFeNiMn)_{(100-x)}Co_x$ HEAs exhibit almost the same value of hardness, which may be attributed to the small volume fraction of sigma phase.

Differed from the $(CoCrFeMn)_{(100-x)}Ni_x$ and $(CrFeNiMn)_{(100-x)}Co_x$ HEAs with a single FCC phase, CoCrFeNiAl HEAs have BCC structures, exhibiting relatively high hardness as shown in Fig. 3b. The hardness of $(CoCrFeAl)_{(100-x)}Ni_x$

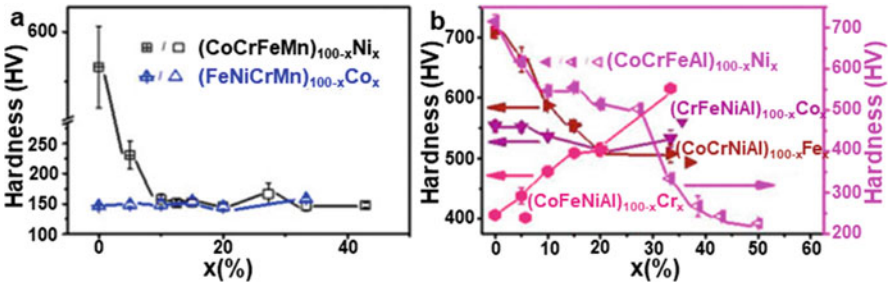

Fig. 3 Hardness of the as-cast (**a**) $(CoCrFeMn)_{(100-x)}Ni_x$ and $(CrFeNiMn)_{(100-x)}Co_x$ HEAs, and (**b**) $(CoCrFeAl)_{(100-x)}Ni_x$, $(CrFeNiAl)_{(100-x)}Co_x$, $(CoCrNiAl)_{(100-x)}Fe_x$, and $(CoFeNiAl)_{(100-x)}Cr_x$ HEAs. The legend "+" centred symbols denote multiple phases, fully open symbols represent either single or duplex FCC phases, fully closed symbols denote duplex BCC phases, and left-half open symbols represent FCC and duplex disordered plus ordered BCC phases [28]

HEAs decreases since phase transformation from BCC to FCC structures occurs with increasing Ni concentration. Even though the $(CoCrNiAl)_{(100-x)}Fe_x$, $(CoFeNiAl)_{(100-x)}Cr_x$ and $(CrFeNiAl)_{(100-x)}Co_x$ HEAs have similar BCC structures, their variation trends of hardness are different. With the increase of x value, the hardness value of $(CrFeNiAl)_{(100-x)}Co_x$ and $(CoCrNiAl)_{(100-x)}Fe_x$ HEAs decreases, while that of $(CoFeNiAl)_{(100-x)}Cr_x$ increases. As mentioned by Zhu et al. [28], the different variation trends of hardness among different HEAs may be due to the different bond energies, which need further investigation. Therefore, an optimal design of HEAs with desired hardness is a complicated task, which can be especially challenging for trial-and-error experimental developments. This is where an ML approach could provide some valuable insights.

1.3.2 Strength and Ductility Synergy

Metallic materials have been widely used as structural materials, where the strength and ductility are two baseline mechanical properties. The goal is to achieve high strength and high ductility in such materials as much as we can, which is challenging since these two properties often exhibit a trade-off, i.e., a gain in strength usually induces a sacrifice in ductility. Heterogeneities have been intentionally introduced into conventional metals/alloys, such as a grain/twin size gradient, lamellae thickness gradient, and phase structure gradient [29], to promote strain hardening and hence uniform tensile ductility, achieving considerably improved strength–ductility synergy. Motivated by the role of heterogeneities in conventional metals/alloys, researcher also tailored heterogeneities in HEAs to promote strength–ductility synergy.

Ma et al. [12] categorized the heterogeneities in HEAs into multiple levels. The first level arises from the multiple principal elements at the atomic level, i.e., the compositional and packing arrangements of various elemental atoms (short−/medium-range ordering in the neighbour shells). For example, Ding et al. [30] synthesized a CrFeCoNiPd HEA, where all five elements formed atomic aggregation with a wavelength of 1–3 nm. This heterogeneity exhibited considerable resistance to dislocation glide, leading to higher yield strength without compromising ductility. The next level of heterogeneity refers to the nanoscaled clusters, complexes, or precipitates. For example, Lei et al. [31] doped a TiZrHfNb HEA with 2.0 atomic percent oxygen, leading to a strength–ductility synergy with tensile strength improved by 48.5 ± 1.8% and ductility enhanced by 95.2 ± 8.1%. The underlying mechanism is that oxygen tends to form ordered interstitial complexes, changing the dislocation shear mode from planar slip to wavy slip, promoting double cross-slip and dislocation multiplication during deformation.

The third level of heterogeneity comes from multi-phase structures that evolve from a single-phase solid solution, including transforming to dual phase, eutectic lamellae structure, martensites, etc. For example, Shi et al. [32] synthesized a $AlCoCrFeNi_{2.1}$ eutectic HEA (EHEA) with a dual-phase heterogeneous lamella (DPHL) structure. Mechanical properties of the DPHL HEAs and various reported superior metallic materials are compared in Fig. 4. Both Shi et al.'s DPHL HEAs [32] and other reported HEAs [33–39] are separated from the general trend of conventional metallic materials for the tensile strength-elongation map (Fig. 4a), suggesting a promoted strength–ductility synergy in HEAs. However, in the yield strength-elongation map (Fig. 4b), only Shi et al.'s HEAs [32] stand out from the trend, with yield strength of ~1.5 GPa and elongation of ~16%. Due to phase decomposition, there are substantial hard intergranular ordered BCC phases in the soft FCC lamella matrix to impart an additional rigid deformation constraint to FCC grains, thereby strengthening the HEAs. Moreover, the as-prepared EHEAs can activate microcrack-arresting mechanisms to further extend their strain-hardening ability for improved ductility.

The fourth level originates from the defects in the crystal structures and the grain-size distribution with a length scale from nanometre to micrometre. For example, Wu et al. [40] designed an $Al_{0.1}CoCrFeNi$ HEA by combining non-recrystallized and recrystallized grains in heterogeneous structures, which exhibits enhanced strength-ductility synergy from both the underlying plastic accommodation and hardening processes (dislocation hardening, back-stress hardening and twinning). The above multiple levels of heterogeneities in HEAs, leading to lattice friction and back stress hardening, can be utilized as efficient strategies to enhance the strength–ductility synergy of HEAs. The high strength and good ductility provide great potentials for HEAs to outperform conventional metals/alloys in numerous fields, such as civilian infrastructure, transportation, and aerospace.

1.3.3 High-Temperature Properties

To develop novel HEAs with desired properties for high-temperature applications has been one of the major interests of the HEA research community. Among the various HEAs, those consisting of refractory elements, i.e., refractory HEAs, have been of particular interest due to their high strength at elevated temperatures. For example, Senkov et al. [41] produced single BCC phase NbMoTaW and VNbMoTaW refractory HEAs, with yield strengths as high as 400–500 MPa at 1600 °C. Strength retention at elevated temperatures has drawn a large amount of attention. However, the densities of refractory HEAs are usually very high, such as 13.8 g/cm^3 for NbMoTaW HEA, and 12.4 g/cm^3 for VNbMoTaW HEA, and refractory HEAs often exhibit an inferior elongation to fracture at room temperature.

To reduce density and enhance ductility at room temperature, the high-density constituents can be substituted by some lower density ones. For example, HfNbTaTiZr HEA (with density of 9.94 g/cm^3) exhibits a high compression yield strength of 929 MPa and a superior room temperature ductility greater than 50% [42]. To further increase the high-temperature strength and decrease the density of HfNbTaTiZr HEA, different strategies could be adopted, e.g., by adding low-density elements like Mo, Cr, and Al [43, 44] or alternatively by adding Si so that a low-density secondary phase could be formed [45]. For example, Juan et al. [46] enhanced the yield strength from 100 to 550 MPa at 1200 °C by adding Mo in HfNbTaTiZr HEA, while maintaining a reasonable room temperature ductility of 12%. To date, the refractory HEA family mainly consists of eleven elements: Hf, Nb, Ta, Ti, Zr, V, W, Mo, Cr, Al, and Si. Other refractory elements, such as Ir, Os, Re, Rh, and Ru, have not yet been utilized in refractory HEAs.

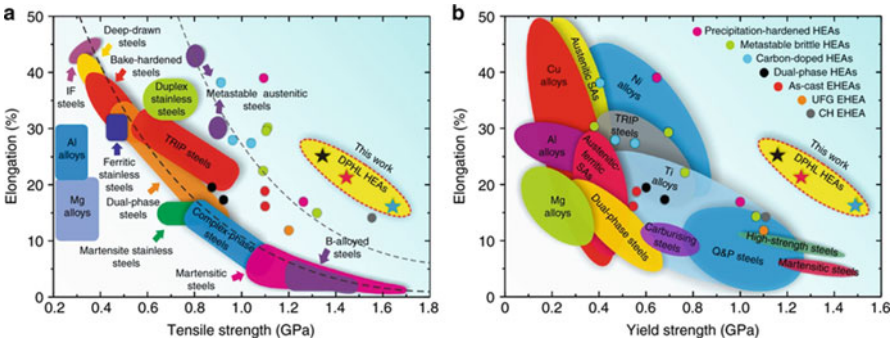

Fig. 4 (**a**, **b**) Mechanical properties of dual-phase heterogeneous lamella (DPHL) HEAs [32] in comparison with conventional metallic materials and other HEAs, including precipitation-hardened HEAs [33], metastable brittle HEAs [34], carbon-doped HEAs [35], dual-phase HEAs [36], as-cast eutectic HEA (EHEA) [37], ultrafine-grained (UFG) EHEA [38], complex and hierarchical (CH) EHEA [39]

2 Computational Modelling and Machine Learning Approaches for High-Entropy Alloys

The huge elemental and compositional space of HEAs provides great opportunities to discover new HEAs with desired properties. Meanwhile, the large unexplored material search space is also challenging for the conventional experimental/simulation techniques in the field. Data-driven ML approaches provide an accurate, computationally inexpensive, interpretable, and transferable way to rapidly screen a given search space to identify the most promising material candidates. In the past few decades, substantial advancement of ML algorithms has expanded the application of data-driven approach throughout science, commerce, and industry. One of the challenges in utilization of ML approaches for material discovery is the lack of large experimental datasets, especially in the space of HEA materials. This problem can be mitigated through computational methods. In this section, we will introduce some of the computational methods and ML approaches for HEA design. Computational methods for HEA design are discussed in Sect. 2.1. Some ML predictions of phase formations are introduced in Sect. 2.2, and examples of ML predictions of mechanical properties are summarized in Sect. 2.3.

2.1 Conventional Computational Methods for HEA Design

To accelerate the discovery and development of HEAs, high-throughput computations and multi-scale simulations are in demand. Computational methods can be utilized to investigate the HEAs spanning different time/length scales and to describe the structural and physical characteristics of materials qualitatively/quantitatively, assisting researchers to understand the materials from multiple aspects. High-throughput calculations can also complement the experiment to provide substantial data for ML models. Computational methods, like experimental techniques, can concentrate on different features of the material, such as different levels of structure descriptions (from atomic level to nanoscale, and to macroscale), as well as various properties (mechanical, physical, or chemical behaviour), etc. Thus, different computational methods targeting different mechanisms have been developed: density functional theory (DFT), molecular dynamics (MD), Monte Carlo (MC), discrete dislocation dynamics (DDD), phase-field method (PFM), thermodynamics model (TM), finite element method (FEM), as well as calculation of phase diagram (CALPHAD). Below we will discuss three most widely used computational methods for HEA design: DFT calculation, MD simulation, and CALPHAD modelling.

2.1.1 DFT Calculation

Generally, first-principle calculation aims to solve the Schrodinger equation with structures and atoms as the input. The Schrodinger equation, however, often has difficulties describing a complex system, and is often limited to dealing with sufficiently simple systems. To simplify the Schrodinger equation, DFT [47, 48] has emerged as one of the most popular first-principle methods. The DFT simplifies the problem of multi-electrons to that of a single electron, describes physical properties of the ground state based on the ground state electron density, and has been extensively employed to study the microstructures and properties of HEAs [49]. Plane-wave-based methods are widely utilized to solve the Kohn–Sham equation for the total energy and force of a HEA system, after which the cell structure and atomic positions are both updated towards the equilibrium state using a structural optimization algorithm. Green's function is also a powerful approach to handling the Kohn–Sham equation within a self-consistent effective medium model.

In principle, a large supercell is required to simulate a HEA, which is extremely difficult for DFT. Although DFT has already employed many simplifications in solving the Schrodinger equation, the computational cost is still quite expensive for HEA systems that consist of multiple constituents. Fortunately, the cluster expansion theory can be employed to utilize a small cell to model the large supercell. For example, one of the popular methods is the specific quasirandom structure (SQS) [50], which allows to capture the chemical disorder and to simulate the local relaxation effects via optimizing the atomic distribution by satisfying the objective functions, including pair correlation, three-body correlation and all the way to many-body correlation, etc., within the neighbouring shells of a solid solution. Moreover, Jiang et al. [51] reported a small set of ordered structures (SSOS) approach to capture the random structures of HEAs, achieving a good accuracy yet with significantly reduced computational cost. For example, an SSOS-3 $\times$ 5 containing only three 5-atom cell structures (Fig. 5a–c) can perfectly match 20 pair correlation functions of the random BCC five-element HEA for the first- and second-nearest neighbours. To achieve the same level of accuracy, it is necessary to use a much larger 125-atom structure in the SQS approach (Fig. 5d).

2.1.2 MD Simulation

Molecular dynamics is a computational method capable of simulating the movements of atoms/molecules (defined as particles). The particles interact with each other and move to energetically favourable sites, capturing a dynamic evolution of the simulated system. The forces exerted on the particles and the system energies are calculated according to the interatomic potentials. The trajectories of particles are updated by solving Newton's equations of motion for each particle numerically. MD simulations are capable of relating atomic-level structures to microscopic behaviours, which have a very extensive range of applications, such as for predicting the mechanical and thermal properties of HEAs [52–54]. Compared with DFT

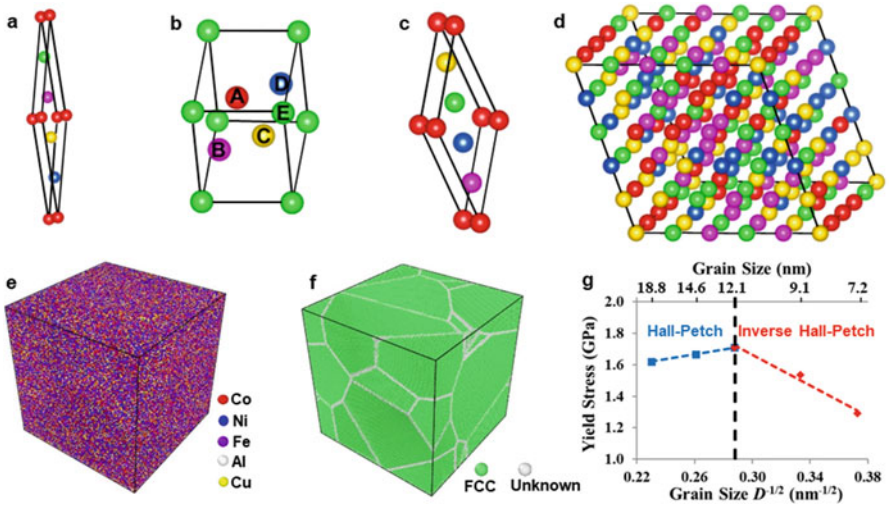

Fig. 5 Three 5-atom cell structures in SSOS-3 × 5 for DFT calculation are shown in (**a**–**c**), respectively. A 125-atom SQS structure for DFT calculation is shown in (**d**) [51]. Polycrystalline model of $CoNiFeAl_{0.3}Cu_{0.7}$ for MD simulation where colour indicates (**e**) atom type and (**f**) phase as determined from common neighbour analysis. (**g**) Variation of yield strength with average grain size for polycrystalline $CoNiFeAl_{0.3}Cu_{0.7}$ HEA under compression along the x direction by MD simulation [52]

calculations, MD simulations can handle much larger time and length scales. MD simulation can also be combined with MC simulation to further extend the simulation scales [8].

HEAs with FCC structures always possess a low yield strength in the range of 200–600 MPa [55]. To tackle this issue, Fu et al. [56] synthesized a nanocrystalline $CoNiFeAl_{0.3}Cu_{0.7}$ HEA with a single FCC phase. This HEA exhibited an amazing yield strength of 1.8 GPa, which was remarkably higher than that of other FCC structured HEAs [55]. To reveal the deformation mechanisms in Fu et al.'s experiments [56], Li et al. [57] performed MD simulations to investigate the compressive process of nanocrystalline HEA with the same composition and similar grain size, from which they concluded that the high strength were associated with a strain-induced phase transformation from FCC to BCC structures. The phase transformation in HEA occurs when the stress induced by severe lattice distortion and external loading exceeds the critical stress required for the nucleation of BCC phase in the matrix.

Chen et al. [52] systematically investigated the phase stability, mechanical properties, and deformation mechanisms of $CoFeNiAl_xCu_{1-x}$ ($x = 0.1$–0.9) HEAs. Cohesive energy data demonstrate that, when Al concentrations is low ($x < 0.4$), FCC structure is more stable. Otherwise, BCC structure is more stable. Hall-Petch and inverse Hall-Petch relations were obtained in both FCC and BCC HEAs (FCC $CoNiFeAl_{0.3}Cu_{0.7}$ HEA is shown in Fig. 5e–g). Microstructural evolutions indicate

that the dominant deformation mechanisms are dislocation slip and deformation twinning in the Hall-Petch regime of FCC HEA because of the low stacking fault energy. In contrast, the deformation mechanism of BCC structures is phase transformation. For the inverse Hall-Petch relation, the deformation mechanisms are grain rotation and grain boundary migration for both FCC and BCC HEAs.

2.1.3 CALPHAD Modelling

Different from DFT calculation and MD simulation, CALPHAD [58] is used to perform thermodynamic and kinetic calculations to obtain the phase diagrams and thermodynamic properties of HEAs according to the thermodynamic databases. Phase diagrams play a key role in understanding the HEA formation and usually refer to a graph with axes for composition and temperature of a HEA system, displaying regions where different single phases are stable and where two or more of them coexist. CALPHAD calculations also allow to investigate the phase compositions, fractions, and stabilities as a function of constituents, pressures, and temperatures. This is a powerful tool for predicting the HEA structure under different conditions, providing not only rational guidance for experimental preparation but also substantial data for ML models. Besides, CALPHAD can be used to predict the thermodynamic properties for each phase and multiple phases.

A reliable thermodynamic database is a prerequisite for CALPHAD modelling of HEAs. Gao et al. [3] stated that the top priority in establishing a reliable database of HEAs is to gather the phase-equilibrium data from the lower-order alloy systems, i.e., the corresponding binaries and ternaries. Unfortunately, such experimental data are usually not sufficient. Fortunately, DFT calculations and MD simulations often can complement experiment to fill up the thermodynamic data. To date, several commercial software with robust thermodynamic database are available, such as Thermo-Calc [59], Pandat [60], and FactSage [61]. In particular, the TCHEA database [59] developed for HEAs includes all the binary and most ternary systems associated with 26 elements, while the PanHEA database [60] contains all the binary and ternary systems related to HEAs consisting of Al, Co, Cr, Cu, Fe, Mn, and Ni, providing unprecedented possibilities for computational method assisted discovery of HEAs.

MacDonald et al. [62] employed Thermo-Calc's TCHEA database to perform systemic analysis by comparing the CALPHAD-predicted phases and the experimentally observed phases in the CoCuFeMnNi HEA. Figure 6a plots a step diagram with the equilibrium phases over a range of temperatures predicted by CALPHAD. This diagram indicates a disordered FCC phase with all the constituent elements (labelled as L12#2 in red) from the melting temperature (1157 °C) to 727 °C. A Cu-rich disordered FCC phase (labelled as L12 in green) is predicted from low temperature to 727 °C, and an Fe-Co-rich B2 phase (labelled as B2 in light blue) is predicted from low temperature to 559 °C. The step diagram agrees with the experimentally observed phases well, except for some errors in the precise temperature points at which the phases form.

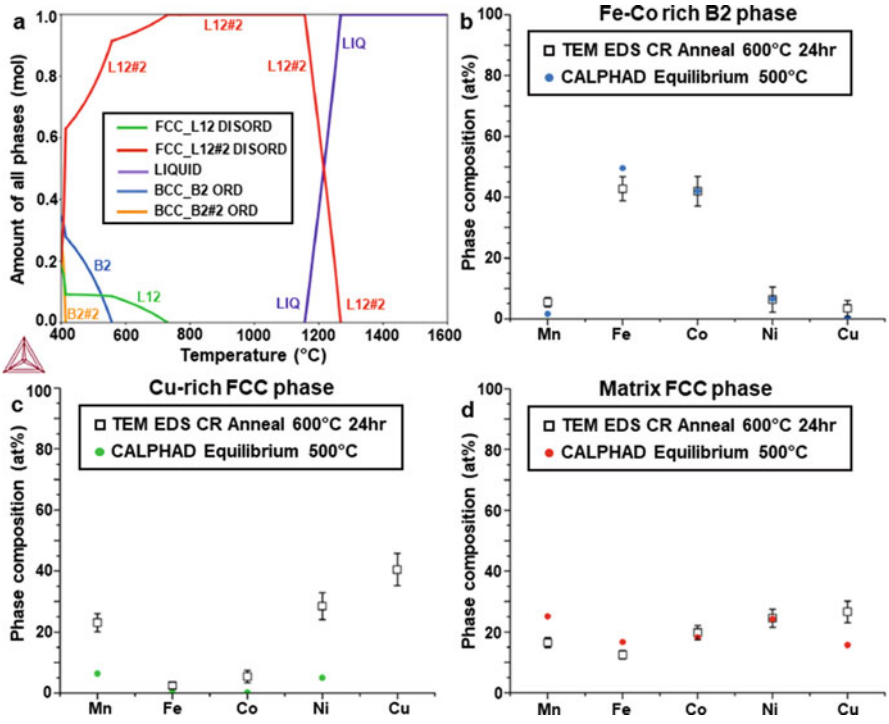

Fig. 6 (**a**) Phase diagram of the CoCuFeMnNi HEA in the temperature range of 400–1600 °C predicted by CALPHAD. Phase compositions by CALPHAD predictions and experimental measurements for the three phases: (**b**) Fe-Co-rich B2 phase, (**c**) Cu-rich FCC phase, and (**d**) matrix FCC phase [62]

The coarsening of secondary phases during post deformation annealing treatment at 600 °C for 24 h allows for quantitative energy dispersive X-ray spectrometer measurements of each phase observed. These experimental measurements are compared with the CALPHAD predicted compositions of each phase at 500 °C in Fig. 6b–d, since 500 °C is the highest temperature that CALPHAD predicts the formations of all three phases. For the compositions of the ordered Fe-Co B2 phase (Fig. 6b) and the matrix disordered FCC phase (Fig. 6d), the predicted data are in relatively good agreement with experimental data. The experimental Cu-rich phase contains dramatically higher compositions of Ni and Mn than CALPHAD predicted. This trend indicates that the modelling of a segregating element in an HEA appears to be unreliable in Thermo-Calc software with this TCHEA database [62]. ML approaches are likely to provide guidance in addressing this inconsistence.

2.2 Machine Learning Predictions of Phase Formations

The intrinsic property of an HEA highly depends on the phase structure: single solid-solution phase (FCC, BCC or HCP), intermetallic compound or amorphous phase. Therefore, accurate prediction of the resulting phase for a given elemental composition is crucial to the rational design and development of new HEAs. Computational methods, such as DFT and CALPHAD, have been employed for predicting the phase formation. However, these methods are not always efficient for a large search space of HEAs. Based on experimental data, parametric methods with various empirical thermo-physical parameters, such as entropy of mixing, enthalpy of mixing, valence electron concentration, and atomic size difference, have been used to make predictions of phase formations [1]. However, these empirical rules only provide limited representation capability and their performance is not always satisfactory. In contrast to conventional computational and parametric methods, data-based ML can improve both the accuracy and efficiency of predictions for HEAs. We will discuss some of ML predictions on single phase (FCC, BCC & HCP), intermetallic compound, and amorphous phase of HEAs below.

2.2.1 Single-/Multi-Phase Solid Solution

Yeh et al. [1] proposed that equimolar compositions maximize the configurational entropy of HEAs, stabilizing the formation of solid-solution (SS) phase. This trend indicates that the possibility for the SS formation in HEAs increases with the number of constituent elements increasing. However, it is well known that the SS formation in HEAs does not merely depend on the elemental quantities [5]. The Hume-Rothery rules [63] have been widely used to predict the SS formations of binary alloys, indicating that the misfit in the features of constituent elements strongly influences the SS formations in binary alloys. For HEAs, King et al. [64] proposed an empirical rule, correctly predicting the formation and stability of 177 single-phase structures of the 185 experimentally reported HEAs. However, the empirical rules for the prediction of SS formation proposed so far usually have very compromised predictability [65].

Motivated by this idea, Pei et al. [65] performed an ML study with a large dataset (1252 samples) and showed that the SS formations could be quite accurately predicted (93%). The dataset for ML consisted of 625 single-phase and 627 multi-phase samples from binary to quinary alloys, whose compositions, phase structures, and thermodynamic properties were obtained from CALPHAD modelling, DFT calculation, and hybrid MC/MD simulation [66]. The descriptors used for ML were elemental properties, whose pair correlations with alloy phases are shown in Fig. 7a. The correlation matrix indicates that the elemental properties, such as bulk modulus, vaporization heat, and valence, possess quite strong correlations (>0.6). Because most elemental properties exhibit strong correlations with each other (i.e., collinearity), it is impossible to employ a simple linear model to predict the phases

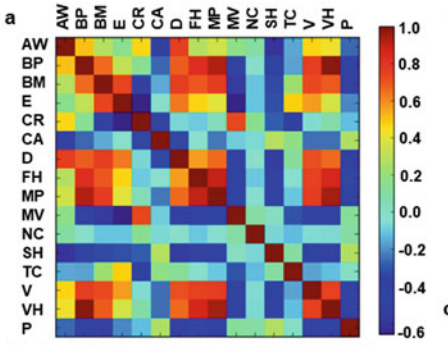

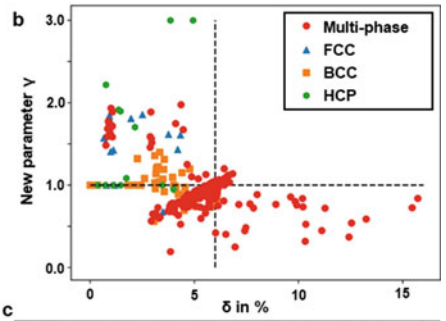

c

Structure	#Single-phase	#Total	Consistency (%)
i. The new rule ≥1 with α = 0.2			
FCC	21	24	88
BCC	27	41	66
HCP	13	14	93
Multi-phase	63	217	71
Average			73
ii. The new rule ≥1 with α = 0.2 jointly with δ ≤ 6%			
FCC	21	24	88
BCC	27	41	66
HCP	13	14	93
Multi-phase	38	217	82
Average			81

d

Group	New rule γ ≥ 1	CALPHAD	Consistency (%)
FCC	5	5	100
BCC	71	67	94
HCP	1	0	0
Summary	77	72	94

Fig. 7 (**a**) The correlation matrix of elemental properties with alloy phases. (**b**) The variation of new parameter γ with lattice misfit δ. The values of $\gamma \geq 3$ are tuned to 3 for better visualization. (**c**) The predictability of the new rule when $\gamma \geq 1$ with $\alpha = 0.2$ (*i*) only and (*ii*) hybrid with $\delta \leq 6\%$. (**d**) Validation of the new rule $\gamma \geq 1$ with $\alpha = 0.2$ rule by CALPHAD method [65]

accurately. It is obvious that simple pair correlations are not robust to map elemental properties to the phases; hence a nonlinear ML model is highly demanded.

Nonlinear Gaussian process is a powerful ML algorithm, which has led to high predictability with an accuracy of 93% [65]. For ML predictions of phase formations, Pei et al. [65] identified the most important descriptors: molar volume, bulk modulus, and melting temperature. By utilizing these descriptors, a new thermodynamics-based rule was developed to predict SS phases, with a new parameter γ calculated as the ratio of Gibbs free energy of N-component alloys to the lowest Gibbs free energy of its binaries. If $\gamma \geq 1$, a single-phase solid solution is predicted to form. The ML prediction results are shown in Fig. 7b, c, which accurately predicts 88% FCC, 66% BCC, and 93% HCP alloys with an optimized parameter $a = 0.2$. The average accuracy is 73% by the empirical rule alone. If it is hybrid with the empirical rule of atomic size misfit $\delta \leq 6\%$, the accuracy increases to 81%, giving much better predictability than by the rule alone. To test the predictability of this rule, the phase structures of new alloys were also predicted and compared with CALPHAD modelling. The high consistency between CALPHAD and ML in Fig. 7d indicates that Pei et al.'s rule [65] obtained from ML can act as a guide to discover HEAs with desired phase structures.

By coupling thermodynamic and chemical features with a random forest model, Kaufmann et al. [67] also proposed a high-throughput ML approach to predict the single- or multi-phase SS formation. The dataset contained a total of 1798 unique samples with equimolar compositions from Lederer et al.'s DFT calculations [68]. The 1798 samples consisted of 117 binaries, 441 ternaries, 1110 quaternaries, and 130 quinaries. The ML prediction accuracy for the binary, ternary, quaternary, and quinary samples were 87.2%, 63.3%, 62.2%, and 72.3%, respectively. The incorrect predictions were found to be related to the lack of training data for the ternary compositions as well as the absence of compositions that were not single-phase BCC or FCC in the quaternaries and quinaries. This model can be employed as a primary tool or integrated into existing alloy discovery workflows to explore material space in an unconstrained manner and to predict the results of new experiments.

With an experimental dataset containing 322 as-cast samples consisting of ternary to nonary multi-principal element alloys, Li et al. [69] built a support vector machine model to distinguish the FCC, BCC single phases, and the remaining phases, achieving a cross-validation accuracy over 90% after training and testing. Five elemental properties, i.e., atomic size difference, valence electron concentration, configurational entropy, mixing enthalpy, and melting temperature, were selected as descriptors to reduce the risk of overfitting. With this model, the phases of 267 BCC and 369 FCC equimolar HEAs in the composition space of 16 metallic elements were further predicted. Interestingly, dozens of refractory HEAs possessing high ratios of melting point to density have been sought out. In particular, 11 of them are well consistent with the experimental measurements [70–72]. Besides, 20 quinary refractory HEAs with highest melting points also agree well with DFT calculations. This proposed ML model complements the calculation of phase diagrams and provides useful guidance for designing new HEAs.

2.2.2 Solid-Solution, Intermetallic, and Amorphous Phases

Beside the above SS phase, diverse other phases, such as intermetallic (IM) compound or amorphous phase (AM), also appeared in HEAs. Based on ML algorithm, Zhou et al. [73] examined the commonly used design rules for HEA phases. The dataset used for ML contained 601 as-cast alloys with 131 SS alloys, 248 IM alloys, 165 AM alloys, 6 mixed IM and AM alloys, and 51 mixed SS and IM alloys. The descriptors contained 13 parameters, including mean atomic radius (a), atomic size difference (δ), electronegativity (χ), standard deviation of electronegativity ($\Delta\chi$), average valance electron concentration (VEC), standard deviation of VEC (σ_{VEC}), average mixing enthalpy (ΔH_{mix}), standard deviation of mixing enthalpy ($\sigma_{\Delta H}$), ideal mixing entropy (S_{id}), average of the melting temperatures of constituent elements (T_{m}), standard deviation of melting temperature (σ_{T}), mean bulk modulus (K), and standard deviation of bulk modulus (σ_{K}).

Figure 8 shows a comparison of sensitivity measures of the 13 descriptors for AM, IM, and SS phases, which are coloured according to the ratio of mean to standard deviation. Red colour stands for positive correlation, while blue colour for

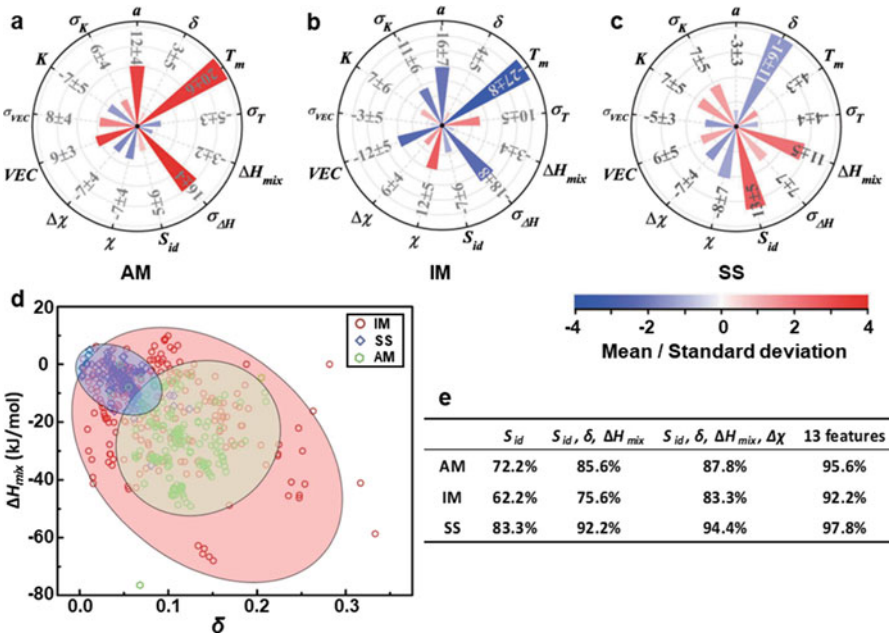

	S_{id}	S_{id}, δ, ΔH_{mix}	S_{id}, δ, ΔH_{mix}, $\Delta\chi$	13 features
AM	72.2%	85.6%	87.8%	95.6%
IM	62.2%	75.6%	83.3%	92.2%
SS	83.3%	92.2%	94.4%	97.8%

Fig. 8 The sensitivity measures of 13 design parameters for (**a**) amorphous (AM), (**b**) intermetallics (IM), and (**c**) solid-solution (SS) phases. (**d**) The plot of δ vs. ΔH_{mix} for SS, IM, and AM. (**e**) Comparison of the accuracy of 1-descriptor, 3-descriptor, 4-descriptor, and 13-descriptor model [73]

negative correlation. The sensitivity measure of S_{id} for SS is highly positive (+13 in Fig. 8c), while that for IM is quite negative (−7 in Fig. 8b). Figure 8c indicates that a higher value of S_{id} tends to form SS phase, which is consistent with the high entropy effect. In particular, the sensitivity measure of S_{id} is positive for AM (+5 in Fig. 8a), suggesting that increasing the chemical complexity does promote glass formation. Figure 8c also shows that δ has a remarkable influence on the SS formation, whereas ΔH_{mix} and S_{id} exhibit similar degrees of influence on the SS formation. The highly negative value of δ (−16 in Fig. 8c) indicates that the atomic size mismatch needs to be minimized in order to obtain SS phase.

As shown in Fig. 8d, SS has a narrower distribution of δ and ΔH_{mix} than AM and IM, indicating that SS is more related to the variation of δ or ΔH_{mix} as compared with IM and AM. It also demonstrates that increasing δ will promote AM and IM and inhibit SS, which is consistent with the negative values of δ for SS in Fig. 8c (−16). For a quantitative comparison, ML prediction accuracies with different sets of descriptors are estimated and compared in Fig. 8e. Clearly, ML model with a single parameter S_{id} exhibits the poorest accuracy, as low as ~62% for IM. Generally, the addition of other elemental properties as descriptors, such as δ, ΔH_{mix}, and $\Delta\chi$, increases the prediction accuracy for all three phases. Therefore, the ML model with all elemental properties (13 descriptors) is better than the other

models with only partial design parameters. The extremely high accuracy for the best ML model (95.6% for AM, 92.2% for IM, and 97.8% for SS) demonstrates that the ML approach is a powerful tool for designing HEAs with desired phase structures.

Using a comprehensive experimental dataset summarized in the review article of HEAs [4], including 401 different HEAs with 174 SS, 54 IM, and 173 mixed SS and IM (SS + IM) phases, Huang et al. [74] also employed ML algorithms to explore phase selection rules. Three popular ML algorithms, i.e., support vector machine (SVM), K-nearest neighbours (KNN), and artificial neural network (ANN), were adopted to screen out the most suitable ML model. Five parameters were employed as descriptors, including VEC, $\Delta\chi$, δ, S_{id}, and ΔH_{mix}. The whole dataset was divided into four nearly equal portions to execute a cross-validation to avoid overfitting. Each portion was utilized as the testing data only once. When one portion of data was used as testing data, the others were training data. Therefore, four times training and testing of the ML model were performed on different subsets of the full data to execute the cross-validation process, creating a robust model with improved accuracy. The final accuracy was calculated as the average value of these four testing results. The testing accuracy for the SVM, KNN, and ANN models are 64.3%, 68.6%, and 74.3%, respectively. Therefore, the trained ANN model outperforms others and is used for the subsequent predictions of new HEAs.

Utilizing a genetic algorithm (GA) to choose the ML model and associated descriptors efficiently, Zhang et al. [75] collected 550 as-cast HEAs with stable phase formation information from literature sources [76] to construct a dataset and performed a systematic framework. Single BCC phase, single FCC phase, and dual FCC and BCC phase were considered as the SS phase, while intermetallic compounds and amorphous phases were regarded as the non-solid-solution (NSS) phase. Nine ML models with combinations of seventy material descriptors were tested, where GA was employed to achieve an efficient search. The optimized classification model exhibited an accuracy up to 88.7% for identifying SS and NSS HEAs and further to 91.3% for distinguishing BCC, FCC, and dual-phase HEAs. With a small dataset of 118 samples, Islam et al. [77] employed neural network ML model to recognize the underlying data pattern and predict the corresponding phase of multi-principal element alloys. The trained ML model reached an accuracy of over 99% for the full dataset, while an average generalization accuracy higher than 80% were obtained for the cross-validation training and testing datasets.

2.2.3 Precipitation

For the precipitation in HEAs, Sato et al. [78] studied the strengthening of ordered $L1_2$ precipitate (γ') in the CoAlW alloy system in 2006, which has sparked the research interest in designing novel γ'-strengthened Co-base superalloys with excellent properties for aircraft applications. For example, Liu et al. [79] proposed an ML strategy to design Co-base superalloys ($Co_aAl_bW_cNi_dTi_eTa_fCr_g$) with multiple targeted properties optimized simultaneously. Among all the properties

that the γ'-strengthened superalloys possess, the γ' solvus temperature is one of the most important, since it reflects the upper limit of temperature capability. Hence, to develop superior γ'-strengthened Co-base alloys, a high γ' solvus temperature (i.e., $T_{\gamma'\text{-solvus}} > 1250$ °C) is essential. Moreover, the targeted processing window ($\Delta T_p = T_{\text{solidus}} - T_{\gamma'\text{-solvus}} \geq 40$ °C), freezing range ($\Delta T_f = T_{\text{liquidus}} - T_{\text{solidus}} \leq 60$ °C), microstructural stability, and density ($\rho \leq 8.7$ g/cm^3) were also optimized simultaneously by Liu et al. [79].

In Liu et al.'s work [79], the quantities of samples in the original dataset were 31, 68, 94, and 134 for the density, liquidus, solidus, and γ' solvus temperature, respectively. With the chemical compositions as the descriptors, six different regression models, including AdaBoost, support vector machine with a kernel of radial basis function, decision tree, k-nearest neighbours, random forest (RF), and gradient tree boosting (GTB) algorithms, were built by Liu et al. [79]. The receiver operating characteristic (ROC) curve was used to evaluate the performance of the ML model, as shown in Fig. 9a. When the ROC curve is closer to the upper left corner of the graph, the model shows better performance. The area under the ROC curve (i.e., AUC value) can also be employed to evaluate the accuracy of ML predictions. The closer the AUC value is to 1, the higher the accuracy of the ML model. The mean value of 100 AUC values for the GTB model is 0.96 and larger than that of other models. The best ML models for predicting the γ' solvus temperature, liquidus, density, and solidus were the GTB, GTB, GTB, and RF, respectively, whose performances on the testing dataset are shown in Fig. 9b–e. Therefore, the GTB model is the best among the six different regression models and chosen as the ML model for the subsequent predictions of new alloys in the potential composition space.

For the $Co_aAl_bW_cNi_dTi_eTa_fCr_g$ alloys, the potential composition space was defined by Liu et al. [79] as: $30\% \leq a \leq 100\%$, $10\% \leq b \leq 15\%$, $1\% \leq c \leq 8\%$, $20\% \leq d \leq 50\%$, $1\% \leq e \leq 8\%$, $1\% \leq f \leq 4\%$, $2\% \leq g \leq 10\%$, where the concentrations of elements were in atomic percent. Each alloy in this space was constrained by $a > d$ to satisfy the concept of Co-base alloys with $a + b + c + d + e + f + g = 100\%$. A series of new Co-base superalloys were screened out successfully and synthesized out of 210,000 candidates experimentally. As shown in Fig. 9f, three iterations were performed in experiments until the as-prepared alloy's γ' solvus temperature was >1250 °C and no longer increased significantly. The best candidate, Co-36Ni-12Al-2Ti-4Ta-1W-2Cr, exhibited the highest γ' solvus temperature (1266.5 °C), a satisfying density of 8.68 g/cm^3, a γ' volume fraction of 74.5%, and excellent high-temperature (1000 °C) oxidation resistance. Thus, ML has provided a new strategy to optimize multicomponent alloys with precipitations to obtain multi-target properties.

For more complicated precipitations in HEAs, Qi et al. [80] classified 600+ reported HEAs for ML based on their phases and precipitations: disordered FCC (A1), disordered BCC (A2), disordered HCP (A3), mixed disordered FCC + BCC (A1 + A2), ordered BCC (B2), disordered solid-solution phases + B2 precipitations (SS + B2), and IM mixed with the other phases (IM+). Single-phase HEA predictions (89–90% success rates) had higher accuracy than mixed

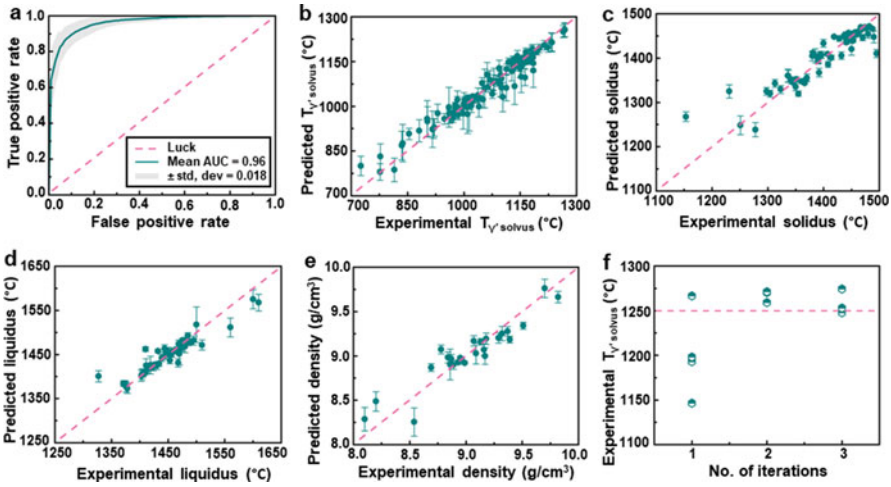

Fig. 9 (**a**) The ROC curve of ML model. The standard deviation of 100 ROC curves is marked in grey, and a random classification is plotted by the pink dashed line. The ML predictions of the best model on the testing dataset as a function of experimental measurements for the (**b**) γ' solvus temperature, (**c**) solidus, (**d**) liquidus and (**e**) density, respectively. The error bars are the standard deviation of 1000 ML predictions. The pink dotted line indicates perfect match, i.e., the ML predictions and experimental measurements are in good agreement. (**f**) The experimental γ' solvus temperature as a function of the number of iterations. The pink dashed line plots the target 1250 °C [79]

phase predictions (78–85% success rates) with 50–90% training sets. Overall, this ML model gave accurate predictions on phase formations, where both the overall predictions and single-phase predictions of HEAs were >80%. Furthermore, 42 new HEAs with randomly selected complex compositions were prepared by suction casting to validate the ML predictions, and 34 out of the 42 HEA samples were correctly predicted by ML, exhibiting an accuracy of 81%. This highly predictive ML approach can be employed to complement experiment in guiding HEA design.

2.3 Machine Learning Predictions of Mechanical Properties

As mentioned above, the huge compositional space of HEAs provides a nice opportunity to improve mechanical properties, such as hardness, yield strength, ductility, Young's modulus, and elastic constant, yet at the same time sets a great challenge in elemental selection and concentration optimization, especially if only explored through trial-and-error type of experiments. ML approach has proven to be a powerful strategy to predict phase formations of HEAs, as discussed in the above section. Here in this section, we discuss some of the ML predictions on hardness, Young's modulus, and elastic constant of HEAs.

2.3.1 Hardness

Hardness is a measure of the resistance to localized plastic deformation induced by mechanical indentation or abrasion. Wen et al. [81] formulated a materials design strategy combining a ML surrogate model with design of experiment (DOE) to search for HEAs with large hardness in AlCoCrCuFeNi HEA system. The dataset consisted of 155 samples, which included 22 quaternaries, 95 quinaries, and 38 senaries, all with measured hardness. The iterative design loops are schematically shown in Fig. 10, where iteration loop I (blue dashed line) only uses composition as descriptor and iteration loop II (red solid line) utilizes both composition and feature as descriptors. A ML surrogate model (Fig. 10c) was trained first based on the dataset with hardness (Fig. 10a) and composition and feature as descriptors (Fig. 10b*1* and b*2*). Then, the obtained ML model (Fig. 10c) was employed to predict the hardness of new HEAs in a virtual search space (Fig. 10d). A utility function was used (Fig. 10e) to select a candidate for experimental synthesis (Fig. 10f) by balancing exploitation (relatively high predicted hardness) and exploration (acceptable predicted uncertainties). The measured hardness of newly synthesized sample was added into the training set (Fig. 10a) to perform the next round of iteration to improve the surrogate model.

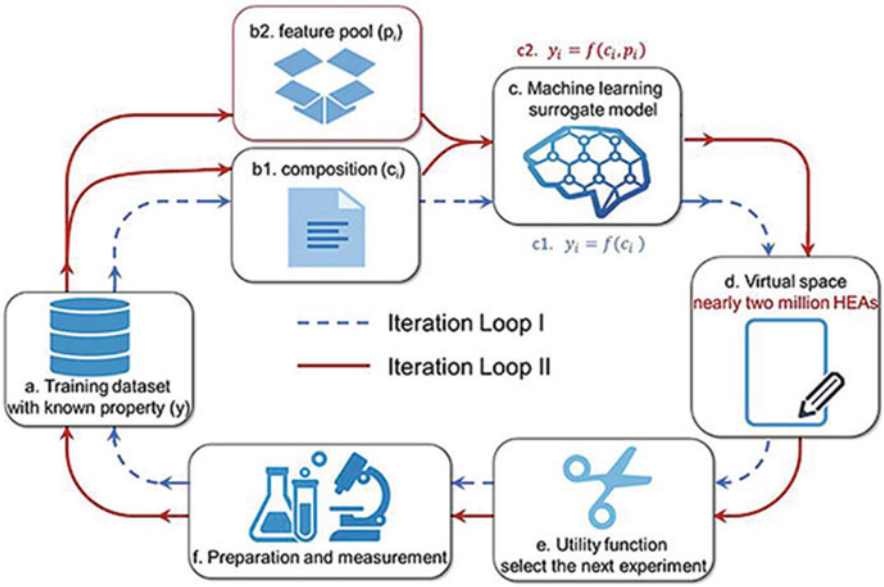

Fig. 10 A schematic of the iteration loop by ML for accelerated discovery of HEAs, including (**a**) dataset construction with hardness, (**b**) descriptor selection (b*1*: composition and b*2*: feature), (**c**) ML surrogate model training, (**d**) new predictions for a search space, (**e**) utility function to choose experimental candidates, and (**f**) experimental preparation and measurement. A feature pool is added into the descriptors of Iteration Loop II, as compared with Iteration Loop I [81]

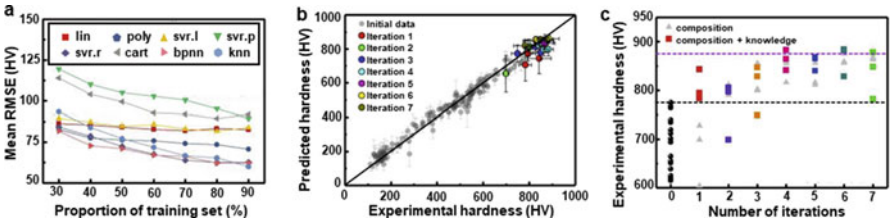

Fig. 11 (**a**) Model evaluation by calculating the mean RMSE for different regression models in Iteration Loop I. The inset enlarges the curves for the three best models of svr.r, bpnn, and knn. (**b**) The predicted hardness values versus the measured ones for samples in the datasets for Iterative Loop II, including the new experimental data during seven iterations. (**c**) The hardness values of the newly synthesized samples during iterations. The inset draws the highest predicted values during iterations. Black and purple dashed lines indicate the best values in the original training dataset and obtained using Iterative Loop I, respectively [81]

For the ML models, Wen et al. [81] used a series of regression algorithms, including linear regression (lin), polynomial regression (poly), back propagation neural network (bpnn), regression tree (cart), k-nearest neighbour (knn), and support vector regression with linear kernel (svr.l), polynomial kernel (svr.p), and radial basis function kernel (svr.r), to predict the hardness. The performance of each ML model in Iteration Loop I was evaluated by calculating the mean root mean square error (mean RMSE) on the testing set, whose results with different split ratios of training and testing sets are shown in Fig. 11a. Overall, the error of each ML model decreased with increasing the size of training set. When the size of training set was 70% and that of testing set was 30%, the svr.r model presented the minimum prediction error. Thus, the svr.r model was selected to predict the hardness of new alloys in the virtual search space for subsequent iterations.

Figure 11b shows the ML predicted hardness as a function of the experimental measurements for all samples from the original dataset and the newly synthesized ones by experiment. The closer the data is to the diagonal line, the more adequate the model is. Figure 11c shows the measured hardness of the newly synthesized samples for Iteration Loop I (labelled as composition in grey) and II (labelled as composition + knowledge in colour). Compared with Iteration Loop I, the samples predicted in the first iteration of Iteration Loop II exhibited higher hardness than all of the original samples. A sample with hardness of 843 HV was discovered for Iteration Loop II, which was 8.8% higher than the highest value in the original dataset. The hardness values obtained in Iteration Loop II were always higher than those in Iteration Loop I during the iterations. The best performer, $Al_{47}Co_{20}Cr_{18}Cu_5Fe_5Ni_5$, possessing the highest hardness, was predicted in the fourth iteration of Iteration Loop II. Its hardness value reached as high as 883 HV, which was 14% larger than the highest value in the original dataset. This strategy offers a recipe to rapidly optimize HEA systems towards desired properties.

For an AlCoCrFeMnNi HEA system by substituting Cu with Mn, Chang et al. [82] utilized an artificial neural network (ANN) model to explore promising

compositions for synthesis of high-hardness HEAs. In the dataset, 91 experimental records composed of targeted elements were collected from literature, including compounds from binary alloys to senary alloys. Simulated annealing (SA), a probabilistic algorithm for approaching the global optimum of a function, was adopted in this work to screen out the candidate with targeted hardness and risk. The ML results demonstrated that the SA algorithm could accelerate the discovery of novel alloys in the unexplored compositional space, by identifying three candidates with hardness >600 HV. In particular, one candidate showed a 20% increase compared with the highest value in the original dataset. The correlations between the predicted composition, hardness, and microstructure were further explored by experiment. Experimental measurements indicate that the evolution of the hardness is related to the phase transition from FCC to BCC + B2.

To design HEAs with high hardness and low density, Menou et al. [83] utilized a multi-objective optimization genetic algorithm combining solid solution hardening (SSH) and CALPHAD modelling with data mining. This approach screened out 3155 alloys that were Pareto-optimal or non-dominated, meaning that no other candidate would form single solid solution and have higher SSH and lower density simultaneously than any one of them. Among the 3155 samples, $Al_{35}Cr_{35}Mn_8Mo_5Ti_{17}$ was chosen for experimental validation by vacuum arc melting. This as-prepared alloy formed a single disordered solid solution, exhibiting a Vickers hardness of 658 HV and a density below 5.5 g/cm^3. This is one of the hardest metals/alloys ever reported for such a low density, demonstrating the promise of ML in discovering novel alloys with multi-objective optimization, as compared with experimental trial-and-error approaches.

2.3.2 Young's Modulus

Young's modulus is a mechanical property that measures the stiffness of a solid material. It defines the relationship between stress (force per unit area) and strain (proportional deformation) in the linear elasticity regime of a material under uniaxial deformation. In the TiMoNbZrSnTa alloy system, Yang et al. [84] formulated a ML approach to explore BCC β-Ti alloys with low Young's modulus (shown in Fig. 12). The dataset was composed of 82 reported β-Ti alloy samples with low Young's modulus from literature, including binary, ternary, quaternary, and quinary alloys in TiMoNbZrSnTa systems. ML algorithms, including random forest (RF), auxiliary gradient-boosting regression tree (XGBoost), and support vector regression (SVR), were trained based on the dataset with Young's modulus and elemental composition. In the forward design (Loop I in Fig. 12), when the alloy compositions are chosen, the Young's modulus can be predicted. Moreover, if the target Young's modulus is set, then alloy compositions can be predicted in the reverse design (Loop II in Fig. 12). To increase the accuracy of ML prediction, some features reflecting the low Young's modulus and β structural stability were implemented into the ML process as descriptors, including the Mo equivalence and the cluster-formula approach, in which the former feature represented the β structural stability, and the

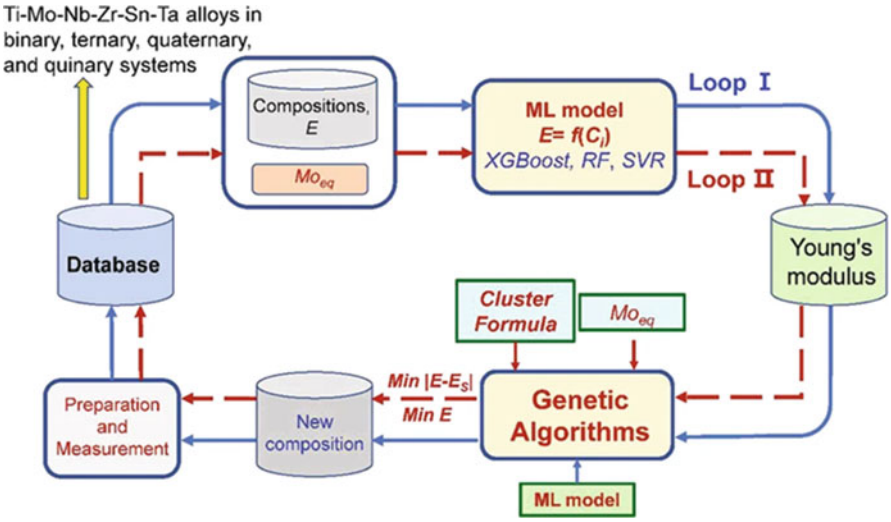

Fig. 12 A schematic diagram for the design loop of multicomponent β-Ti alloys with target Young's modulus in the TiMoNbZrSnTa system by machine learning [84]

latter reflected the interactions among elements. Besides, the genetic algorithm was utilized to handle the nonlinear optimization problem. By setting different objective functions, new alloys were screened out by ML and then validated by experimental preparations and measurements. The newly synthesized samples would be put into the original database for another round of training and prediction.

For the forward design (Loop I), both the RMSE and the coefficient of determination (R^2) were utilized as the criterion for evaluating the prediction accuracy. Since the dataset size of 82 samples was somewhat limited, the multiple hold-out method was employed to ensure accuracy. This process was performed for 500 times in these three models by randomly partitioning samples into training set (90%) and testing set (10%). Figure 13a shows that the mean RMSE values for the training (testing) set are 1.3 ± 0.6 (4.6 ± 0.7) GPa, 3.8 ± 0.3 (4.9 ± 0.9) GPa, and 3.9 ± 0.4 (5.2 ± 0.9) GPa for XGBoost, RF, and SVR methods, respectively. Moreover, Fig. 13b shows that the mean values of R^2 for the training (testing) set are 98 ± 1 (87 ± 2)%, 89 ± 1 (84 ± 4)%, and 88 ± 2 (73 ± 3)% for XGBoost, RF, and SVR, respectively. Therefore, the predicted accuracy of the XGBoost method is higher than those of the RF and SVR methods for the ML prediction of Young's modulus in this alloy system.

For the reverse design (Loop II) of new alloys with low Young's modulus, the evolution histories of the genetic algorithm with the objective function of low Young's modulus are shown in Fig. 13c, d, in which the objective function and the mean value of Young's modulus are plotted as the red and black lines, respectively. These evolution curves indicate that the predicted values are converged to objective values after about 50 iterations to obtain $[(Mo_{0.5}Sn_{0.5})-(Ti_{13}Zr_1)](Nb_{0.5}Ta_{0.5})$

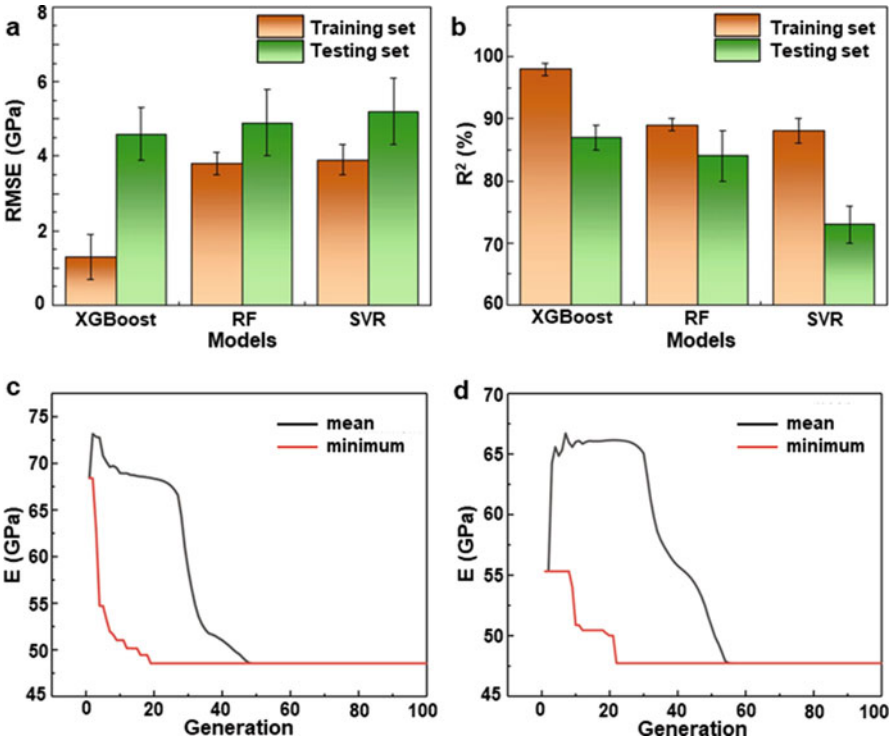

Fig. 13 (**a**) RMSE and (**b**) R^2 values of XGBoost, RF, and SVR methods with 90% training set and 10% testing set. The evolution histories of the genetic algorithm with the objective function of low Young's modulus to obtain (**c**) $[(Mo_{0.5}Sn_{0.5})-(Ti_{13}Zr_1)](Nb_{0.5}Ta_{0.5})$ and (**d**) $[(Mo_{0.3}Sn_{0.7})-(Ti_{13.5}Zr_{0.5})](Nb_{1.5}Ta_{0.5})$ alloys. The objective function and the mean value of Young's modulus are plotted as the red and black lines, respectively [84]

(Fig. 13c) and $[(Mo_{0.3}Sn_{0.7})-(Ti_{13.5}Zr_{0.5})](Nb_{1.5}Ta_{0.5})$ (Fig. 13d) alloys, respectively, indicating a high efficiency of this reverse design. Experimental measurements of Young's modulus for these two predicted new alloys (not included in the original database) indeed reached the minimum values (46–49 GPa). Therefore, this design framework seems capable of predicting high-performance alloys with desired properties including Young's modulus.

For low- (binary), medium- (ternary, quaternary), and high-entropy (quinary) alloys, Roy et al. [85] implemented gradient boost classification model to explore the crystal phase and Young's modulus of an alloy system composed of 5 refractory elements (Mo, Ta, Ti, W, and Zr). The database for phase prediction consisted of 329 samples where 159 entries were BCC phase, 111 entries were FCC phase, and 59 entries were multi-phase, while the database for Young's modulus consisted of only 87 samples because of limited experimental reports. The ML predictions with experimental validations indicate that the electronegativity difference and mean melting temperature contribute most to the phase formation of these refractory

alloys, while the enthalpy of mixing and melting temperature have dominant influences on the Young's modulus of these alloys. Moreover, it also indicates that the entropy of mixing only has negligible impacts on the phase formation and Young's modulus, reigniting the debate on its veritable role in determining the phase and property of HEAs.

2.3.3 Elastic Constants

Elastic constants (e.g., bulk and shear moduli) are parameters that linearly relate stress and strain within the elastic range of a material. As observed in many alloy systems, the elastic constants are closely related to the lattice-distortion-induced strain [86]. It is known that severe lattice distortion naturally exists in HEAs, which may be partly due to the atomic size differences of the constituent elements. For example, the single-phase FCC $Al_{0.3}CoCrFeNi$ HEA, which possesses large size differences among its five types of components, is a typical system to adopt for detailed investigation of the relationship between the elastic properties and lattice distortion. Kim et al. [86] used an integrated experimental and computational approach to explore the elasticity of FCC $Al_{0.3}CoCrFeNi$ HEA based on in situ neutron diffractions, DFT calculations, and ML predictions. It has been reported that, for studying the elastic parameters of HEAs, both Coherent Potential Approximation (CPA) and SQS are generally suitable [87]. Therefore, Kim et al. [86] utilized both CPA and SQS methods to calculate elastic constants for comparison.

The calculated values (SQS and CPA) and experimental measurements (neutron diffraction) for the elastic constants of $Al_{0.3}CoCrFeNi$ HEA are compared in Fig. 14a. Compared with the CPA results, the elastic constants obtained from the SQS method are more consistent with those from neutron-diffraction experiments. The differences between SQS calculations and experimental measurements are within 5% for all elastic constants, indicating reasonable accuracy of the SQS method. To evaluate the effects of lattice distortion on the elastic properties of HEAs, a series of DFT calculations based on a volume-only optimized SQS with atoms fixed on the lattice sites and a fully relaxed SQS structure with the lattice distortion were performed. Figure 14b indicates that the relaxed SQS structure with lattice distortion considered gives more accurate results on bulk and shear moduli, as compared with SQS method with fixed atoms and CPA method. ML was performed using two models, the gradient boosting machine local polynomial regression (GBM-Locfit) and the gradient boosting trees algorithm (GB Trees), with the database containing the results of DFT calculations. The bulk and shear moduli of GBM-Locfit and GB Trees predictions are also plotted in Fig. 14b, indicating that the GB-Trees model exhibits better predictions than the GBM-Locfit model for the bulk modulus. For the shear modulus, GBM-Locfit model overestimated the experimental measurement, while GB-Trees model underestimated the value. This work could inspire more future studies to search for novel alloy based on similar integrated approaches.

Using a similar approach with integrated experimental measurements, theoretical DFT calculations, and ML predictions, Lee et al. [88] also studied the elastic

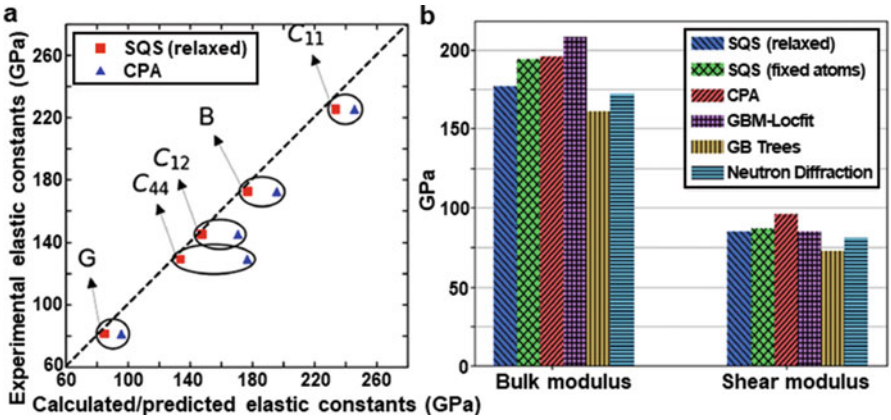

Fig. 14 (**a**) Comparison of experimentally measured and computationally calculated bulk and shear moduli of $Al_{0.3}$CoCrFeNi HEA. (**b**) Comparison of computationally calculated, experimentally measured, and ML predicted bulk and shear moduli

and plastic deformation behaviours of a single BCC NbTaTiV refractory HEA at elevated temperatures. ML models with the GB Trees algorithm were trained based on the DFT-calculated bulk and shear moduli, compound structural information, and elemental properties. A temperature-dependent elastic anisotropic deformation behaviour was revealed by in situ neutron-diffraction experiments. The single-crystal elastic moduli and macroscopic Young's, bulk, and shear moduli were measured by in situ neutron diffraction, with results exhibiting excellent agreement with those from DFT calculations, ML predictions, and resonant ultrasound spectroscopy. The ML predicted shear and bulk moduli were 36.6 GPa and 146.3 GPa with relative errors of 2.5% and 6%, respectively. This work further highlights an integrated experimental and computational approach in the discovery of new HEAs for structural materials applications.

Dai et al. [89] demonstrated that ML can also serve as a powerful tool to help study HEAs through MD simulations. In their work, a deep learning potential (DLP) for high entropy $(Zr_{0.2}Hf_{0.2}Ti_{0.2}Nb_{0.2}Ta_{0.2})C$ was fitted with prediction errors in energy and force being 9.4 meV/atom and 217 meV/Å, respectively. The robustness of the DLP was validated by accurately predicting the variation of structures and properties of mono-phase carbides TMC (TM = Ti, Zr, Hf, Nb, and Ta) with temperature. For example, they were able to predict an increase from 4.5707 to 4.6727 Å in lattice constants, an increase from 7.85×10^{-6} K^{-1} to 10.58×10^{-6} K^{-1} in thermal expansion coefficients, while a decrease from 2.02 $W{\cdot}m^{-1}{\cdot}K^{-1}$ to 0.95 $W{\cdot}m^{-1}{\cdot}K^{-1}$ in phonon thermal conductivities of high entropy $(Zr_{0.2}Hf_{0.2}Ti_{0.2}Nb_{0.2}Ta_{0.2})C$ in temperature ranging from 0 °C to 2400 °C. The predicted properties at room temperature agree well with experimental measurements, demonstrating the accuracy of the DLP. With introduction of ML potentials in MD simulations, one could address many complicated problems that are intractable by conventional computational methods.

3 Summary

This chapter is dedicated to an overview of machine learning approaches and applications for high-entropy alloys, a relatively new class of materials that have attracted considerable interest from the materials research communities in the past decade. Towards this goal, we started by reviewing some of the most fundamental features that characterize HEAs, such as high entropy, sluggish diffusion, severe lattice distortion, and cocktail effects. The high entropy effect tends to stabilize a solid-solution phase as matrix, while the sluggish diffusion effect facilitates accesses to super-saturated states and fine precipitates. The lattice distortion effect improves lattice friction and leads to strength enhancement. The cocktail effect underlines the superior properties beyond the rules of mixture in a multi-principal element alloy. Major preparation methods of HEAs include arc melting, mechanical alloying, and sputter deposition. Arc melting is a dominant preparation method to synthesize bulk HEAs, while sputter deposition is suitable for film/coating deposition. Mechanical alloying has the advantage in alloying of normally immiscible elements. Superior properties of HEAs include high hardness, excellent balance between strength and ductility, and performance under extreme conditions such as high temperature. FCC structured HEAs typically possess a low hardness. By tuning elemental types and concentrations, one can induce phase transformation or precipitate formation to increase the hardness. By tailoring heterogeneities in HEAs, such as short-range ordering, dual phase, and gradient grains, strain hardening and uniform tensile ductility can be substantially enhanced, resulting in considerably improved strength–ductility synergy. Moreover, HEAs consisting of refractory elements can achieve superior high-temperature properties.

Conventional computational methods to investigate the structures and properties of HEAs include DFT, MD, and CALPHAD. DFT calculation is suitable to obtain the energetic data and to predict the structural stability of HEAs by utilizing SQS or SOSS approaches. MD simulation is a powerful method to calculate some of the mechanical and physical properties as well as reveal deformation mechanisms in HEAs, reaching time and length scales way beyond those of DFT. CALPHAD modelling can predict not only the phase compositions, fractions, and stability as functions of composition, pressure, and temperature, but also the thermodynamic properties for each phase and multiple phases. CALPHAD is a powerful tool to relate the HEA structure to property under different conditions, providing not only useful guidance for experimental synthesis but also abundant data for ML approach.

One of the most exciting recent developments in the field is the rapid advance of ML approaches to predict the phase structures and mechanical properties of HEAs. For phase formation in HEAs, accurate predictions of the resulting phases, including solid-solution phase, intermetallic compound, and amorphous phase, can be realized. The database for ML usually comes from both experiment and CALPHAD, reaching thousands of data points. The validated high-performance ML algorithms are Gaussian process, random forest regression, support vector machine, artificial neural network, and gradient tree boosting. The mechanical properties, hardness,

Young's modulus, and elastic constant have all been studied by the ML approach, achieving good accuracy with support vector machine, artificial neural network, or gradient-boosting regression. Compared with phase predictions, the database of property prediction is mostly collected from experiment, whose size is relatively small (typically only hundreds of samples). Therefore, high-throughput experimental or computational methods are desperately needed to provide large amount of data for the ML approach. Although there are abundant studies focusing on HEAs in recent years, current exploration on the structure and property of HEAs is only at the tip of an iceberg. More aspects on microstructures (short−/medium-range ordering), deformation mechanisms (dislocation motion and twinning formation), and thermal properties (melting point and thermal conductivity) still call for ML and other approaches to provide more insights. The huge compositional space of HEAs offers unlimited opportunities for academic and industrial research and development, where ML can be integrated with experimental and simulation methods to accelerate the discovery of next generation materials with unprecedented properties.

References

1. Yeh, J. W., Chen, S. K., Lin, S. J., Gan, J. Y., Chin, T. S., Shun, T. T., Tsau, C. H., & Chang, S. Y. (2004). Nanostructured high-entropy alloys with multiple principal elements: Novel alloy design concepts and outcomes. *Advanced Engineering Materials, 6*(5), 299–303.
2. Cantor, B., Chang, I. T. H., Knight, P., & Vincent, A. J. B. (2004). Microstructural development in equiatomic multicomponent alloys. *Materials Science and Engineering A, 375*, 213–218.
3. Gao, M., Yeh, J., Liaw, P., & Zhang, Y. (2016). *High-Entropy alloys: Fundamentals and applications*. Springer International Publishing AG Switzerland: Springer Nature.
4. Miracle, D. B., & Senkov, O. N. (2017). A critical review of high entropy alloys and related concepts. *Acta Materialia, 122*, 448–511.
5. Zhang, Y., Zhou, Y. J., Lin, J. P., Chen, G. L., & Liaw, P. K. (2008). Solid-solution phase formation rules for multi-component alloys. *Advanced Engineering Materials, 10*(6), 534–538.
6. Takeuchi, A., & Inoue, A. (2001). Quantitative evaluation of critical cooling rate for metallic glasses. *Materials Science and Engineering A, 304*, 446–451.
7. Tsai, K.-Y., Tsai, M.-H., & Yeh, J.-W. (2013). Sluggish diffusion in Co–Cr–Fe–Mn–Ni high-entropy alloys. *Acta Materialia, 61*(13), 4887–4897.
8. Choi, W.-M., Jo, Y. H., Sohn, S. S., Lee, S., & Lee, B.-J. (2018). Understanding the physical metallurgy of the CoCrFeMnNi high-entropy alloy: An atomistic simulation study. *npj Computational Materials, 4*(1), 1–9.
9. Wang, Z., Fang, Q., Li, J., Liu, B., & Liu, Y. (2018). Effect of lattice distortion on solid solution strengthening of BCC high-entropy alloys. *Journal of Materials Science and Technology, 34*(2), 349–354.
10. Tong, Y., Zhao, S., Jin, K., Bei, H., Ko, J., Zhang, Y., & Zhang, F. (2018). A comparison study of local lattice distortion in Ni80Pd20 binary alloy and FeCoNiCrPd high-entropy alloy. *Scripta Materialia, 156*, 14–18.
11. Sohn, S. S., Kwiatkowski da Silva, A., Ikeda, Y., Körmann, F., Lu, W., Choi, W. S., Gault, B., Ponge, D., Neugebauer, J., & Raabe, D. (2019). Ultrastrong medium-entropy single-phase alloys designed via severe lattice distortion. *Advanced Materials, 31*(8), 1807142.
12. Ma, E., & Wu, X. (2019). Tailoring heterogeneities in high-entropy alloys to promote strength–ductility synergy. *Nature Communications, 10*(1), 1–10.

13. Zhang, Y., Zuo, T. T., Tang, Z., Gao, M. C., Dahmen, K. A., Liaw, P. K., & Lu, Z. P. (2014). Microstructures and properties of high-entropy alloys. *Progress in Materials Science, 61*, 1–93.
14. Ranganathan, S. (2003). Alloyed pleasures: Multimetallic cocktails. *Current Science, 85*(10), 1404–1406.
15. Zhang, W., Liaw, P. K., & Zhang, Y. (2018). Science and technology in high-entropy alloys. *Science China Materials, 61*(1), 2–22.
16. Tsao, L., Chen, C., & Chu, C. (2012). Age hardening reaction of the Al0. 3CrFe1. 5MnNi0. 5 high entropy alloy. *Materials & Design (1980–2015), 36*, 854–858.
17. Zou, Y., Ma, H., & Spolenak, R. (2015). Ultrastrong ductile and stable high-entropy alloys at small scales. *Nature Communications, 6*(1), 1–8.
18. Tian, Y., Lu, C., Shen, Y., & Feng, X. (2019). Microstructure and corrosion property of CrMnFeCoNi high entropy alloy coating on Q235 substrate via mechanical alloying method. *Surfaces and Interfaces, 15*, 135–140.
19. Singh, S., Wanderka, N., Murty, B., Glatzel, U., & Banhart, J. (2011). Decomposition in multi-component AlCoCrCuFeNi high-entropy alloy. *Acta Materialia, 59*(1), 182–190.
20. Suryanarayana, C. (2001). Mechanical alloying and milling. *Progress in Materials Science, 46*(1-2), 1–184.
21. Kilmametov, A., Kulagin, R., Mazilkin, A., Seils, S., Boll, T., Heilmaier, M., & Hahn, H. (2019). High-pressure torsion driven mechanical alloying of CoCrFeMnNi high entropy alloy. *Scripta Materialia, 158*, 29–33.
22. Smidt, F. (1990). Use of ion beam assisted deposition to modify the microstructure and properties of thin films. *International Materials Reviews, 35*(1), 61–128.
23. Tsai, M.-H., & Yeh, J.-W. (2014). High-entropy alloys: A critical review. *Materials Research Letters, 2*(3), 107–123.
24. Praveen, S., & Kim, H. S. (2018). High-entropy alloys: Potential candidates for high-temperature applications—an overview. *Advanced Engineering Materials, 20*(1), 1700645.
25. Li, W., Liu, P., & Liaw, P. K. (2018). Microstructures and properties of high-entropy alloy films and coatings: A review. *Materials Research Letters, 6*(4), 199–229.
26. Hsu, C. Y., Wang, W. R., Tang, W. Y., Chen, S. K., & Yeh, J. W. (2010). Microstructure and mechanical properties of new AlCoxCrFeMo0. 5Ni high-entropy alloys. *Advanced Engineering Materials, 12*(1–2), 44–49.
27. Chuang, M.-H., Tsai, M.-H., Wang, W.-R., Lin, S.-J., & Yeh, J.-W. (2011). Microstructure and wear behavior of AlxCo1. 5CrFeNi1. 5Tiy high-entropy alloys. *Acta Materialia, 59*(16), 6308–6317.
28. Zhu, Z., Ma, K., Wang, Q., & Shek, C. (2016). Compositional dependence of phase formation and mechanical properties in three CoCrFeNi-(Mn/Al/Cu) high entropy alloys. *Intermetallics, 79*, 1–11.
29. Li, X., Lu, L., Li, J., Zhang, X., & Gao, H. (2020). Mechanical properties and deformation mechanisms of gradient nanostructured metals and alloys. *Nature Reviews Materials, 5*, 706–723.
30. Ding, Q., Zhang, Y., Chen, X., Fu, X., Chen, D., Chen, S., Gu, L., Wei, F., Bei, H., & Gao, Y. (2019). Tuning element distribution, structure and properties by composition in high-entropy alloys. *Nature, 574*(7777), 223–227.
31. Lei, Z., Liu, X., Wu, Y., Wang, H., Jiang, S., Wang, S., Hui, X., Wu, Y., Gault, B., & Kontis, P. (2018). Enhanced strength and ductility in a high-entropy alloy via ordered oxygen complexes. *Nature, 563*(7732), 546–550.
32. Shi, P., Ren, W., Zheng, T., Ren, Z., Hou, X., Peng, J., Hu, P., Gao, Y., Zhong, Y., & Liaw, P. K. (2019). Enhanced strength–ductility synergy in ultrafine-grained eutectic high-entropy alloys by inheriting microstructural lamellae. *Nature Communications, 10*(1), 1–8.

33. He, J., Wang, H., Huang, H., Xu, X., Chen, M., Wu, Y., Liu, X., Nieh, T., An, K., & Lu, Z. (2016). A precipitation-hardened high-entropy alloy with outstanding tensile properties. *Acta Materialia, 102*, 187–196.
34. Huang, H., Wu, Y., He, J., Wang, H., Liu, X., An, K., Wu, W., & Lu, Z. (2017). Phase-transformation ductilization of brittle high-entropy alloys via metastability engineering. *Advanced Materials, 29*(30), 1701678.
35. Wang, Z., Baker, I., Guo, W., & Poplawsky, J. D. (2017). The effect of carbon on the microstructures, mechanical properties, and deformation mechanisms of thermo-mechanically treated Fe40. 4Ni11. 3Mn34. 8Al7. 5Cr6 high entropy alloys. *Acta Materialia, 126*, 346–360.
36. Baker, I., Meng, F., Wu, M., & Brandenberg, A. (2016). Recrystallization of a novel two-phase FeNiMnAlCr high entropy alloy. *Journal of Alloys and Compounds, 656*, 458–464.
37. Lu, Y., Gao, X., Jiang, L., Chen, Z., Wang, T., Jie, J., Kang, H., Zhang, Y., Guo, S., & Ruan, H. (2017). Directly cast bulk eutectic and near-eutectic high entropy alloys with balanced strength and ductility in a wide temperature range. *Acta Materialia, 124*, 143–150.
38. Wani, I., Bhattacharjee, T., Sheikh, S., Lu, Y., Chatterjee, S., Bhattacharjee, P. P., Guo, S., & Tsuji, N. (2016). Ultrafine-grained AlCoCrFeNi2. 1 eutectic high-entropy alloy. *Materials Research Letters, 4*(3), 174–179.
39. Bhattacharjee, T., Wani, I., Sheikh, S., Clark, I., Okawa, T., Guo, S., Bhattacharjee, P. P., & Tsuji, N. (2018). Simultaneous strength-ductility enhancement of a nano-lamellar AlCoCrFeNi 2.1 eutectic high entropy alloy by cryo-rolling and annealing. *Scientific Reports, 8*(1), 1–8.
40. Wu, S., Wang, G., Wang, Q., Jia, Y., Yi, J., Zhai, Q., Liu, J., Sun, B., Chu, H., & Shen, J. (2019). Enhancement of strength-ductility trade-off in a high-entropy alloy through a heterogeneous structure. *Acta Materialia, 165*, 444–458.
41. Senkov, O., Wilks, G., Miracle, D., Chuang, C., & Liaw, P. (2010). Refractory high-entropy alloys. *Intermetallics, 18*(9), 1758–1765.
42. Senkov, O., Scott, J., Senkova, S., Miracle, D., & Woodward, C. (2011). Microstructure and room temperature properties of a high-entropy TaNbHfZrTi alloy. *Journal of Alloys and Compounds, 509*(20), 6043–6048.
43. Senkov, O., & Woodward, C. (2011). Microstructure and properties of a NbCrMo0. 5Ta0. 5TiZr alloy refractory. *Materials Science and Engineering, 529*, 311–320.
44. Senkov, O., Senkova, S., & Woodward, C. (2014). Effect of aluminum on the microstructure and properties of two refractory high-entropy alloys. *Acta Materialia, 68*, 214–228.
45. Liu, Y., Zhang, Y., Zhang, H., Wang, N., Chen, X., Zhang, H., & Li, Y. (2017). Microstructure and mechanical properties of refractory HfMo0. 5NbTiV0. 5Six high-entropy composites. *Journal of Alloys and Compounds, 694*, 869–876.
46. Juan, C.-C., Tsai, M.-H., Tsai, C.-W., Lin, C.-M., Wang, W.-R., Yang, C.-C., Chen, S.-K., Lin, S.-J., & Yeh, J.-W. (2015). Enhanced mechanical properties of HfMoTaTiZr and HfMoNbTaTiZr refractory high-entropy alloys. *Intermetallics, 62*, 76–83.
47. Hohenberg, P., & Kohn, W. (1964). Inhomogeneous electron gas. *Physical Review, 136*(3B), B864.
48. Kohn, W., & Sham, L. J. (1965). Self-consistent equations including exchange and correlation effects. *Physical Review, 140*(4A), A1133.
49. Ge, H., & Tian, F. (2019). A review of ab initio calculation on lattice distortion in high-entropy alloys. *JOM, 71*(11), 4225–4237.
50. Zunger, A., Wei, S.-H., Ferreira, L., & Bernard, J. E. (1990). Special quasirandom structures. *Physical Review Letters, 65*(3), 353.
51. Jiang, C., & Uberuaga, B. P. (2016). Efficient ab initio modeling of random multicomponent alloys. *Physical Review Letters, 116*(10), 105501.
52. Chen, S., Aitken, Z. H., Wu, Z., Yu, Z., Banerjee, R., & Zhang, Y.-W. (2020). Hall-Petch and inverse Hall-Petch relations in high-entropy CoNiFeAlxCu1-x alloys. *Materials Science and Engineering A, 773*, 138873.

53. Choudhuri, D., Gwalani, B., Gorsse, S., Komarasamy, M., Mantri, S. A., Srinivasan, S. G., Mishra, R. S., & Banerjee, R. (2019). Enhancing strength and strain hardenability via deformation twinning in fcc-based high entropy alloys reinforced with intermetallic compounds. *Acta Materialia, 165*, 420–430.
54. Zhang, Y., Stocks, G. M., Jin, K., Lu, C., Bei, H., Sales, B. C., Wang, L., Béland, L. K., Stoller, R. E., & Samolyuk, G. D. (2015). Influence of chemical disorder on energy dissipation and defect evolution in concentrated solid solution alloys. *Nature Communications, 6*(1), 1–9.
55. Jo, Y., Jung, S., Choi, W., Sohn, S. S., Kim, H. S., Lee, B., Kim, N. J., & Lee, S. (2017). Cryogenic strength improvement by utilizing room-temperature deformation twinning in a partially recrystallized VCrMnFeCoNi high-entropy alloy. *Nature Communications, 8*(1), 1–8.
56. Fu, Z., Chen, W., Wen, H., Zhang, D., Chen, Z., Zheng, B., Zhou, Y., & Lavernia, E. J. (2016). Microstructure and strengthening mechanisms in an FCC structured single-phase nanocrystalline Co25Ni25Fe25Al7. 5Cu17. 5 high-entropy alloy. *Acta Materialia, 107*, 59–71.
57. Li, J., Fang, Q., Liu, B., & Liu, Y. (2018). Transformation induced softening and plasticity in high entropy alloys. *Acta Materialia, 147*, 35–41.
58. Kaufman, L., & Bernstein, H. (1970). *Computer calculation of phase diagrams. With special reference to refractory metals* (Refractory Materials. A Series of Monographs) (Vol. 4). New York: Academic Press Inc..
59. Andersson, J.-O., Helander, T., Höglund, L., Shi, P., & Sundman, B. (2002). Thermo-Calc & DICTRA, computational tools for materials science. *Calphad, 26*(2), 273–312.
60. Chen, S.-L., Daniel, S., Zhang, F., Chang, Y., Yan, X.-Y., Xie, F.-Y., Schmid-Fetzer, R., & Oates, W. (2002). The PANDAT software package and its applications. *Calphad, 26*(2), 175–188.
61. Bale, C. W., Chartrand, P., Degterov, S., Eriksson, G., Hack, K., Mahfoud, R. B., Melançon, J., Pelton, A., & Petersen, S. (2002). FactSage thermochemical software and databases. *Calphad, 26*(2), 189–228.
62. MacDonald, B. E., Fu, Z., Wang, X., Li, Z., Chen, W., Zhou, Y., Raabe, D., Schoenung, J., Hahn, H., & Lavernia, E. J. (2019). Influence of phase decomposition on mechanical behavior of an equiatomic CoCuFeMnNi high entropy alloy. *Acta Materialia, 181*, 25–35.
63. Hume-Rothery, W., & Powell, H. M. (1935). On the theory of super-lattice structures in alloys. *Zeitschrift für Kristallographie-Crystalline Materials, 91*(1-6), 23–47.
64. King, D., Middleburgh, S., McGregor, A., & Cortie, M. (2016). Predicting the formation and stability of single phase high-entropy alloys. *Acta Materialia, 104*, 172–179.
65. Pei, Z., Yin, J., Hawk, J. A., Alman, D. E., & Gao, M. C. (2020). Machine-learning informed prediction of high-entropy solid solution formation: Beyond the Hume-Rothery rules. *npj Computational Materials, 6*(1), 1–8.
66. Gao, M. C., Zhang, C., Gao, P., Zhang, F., Ouyang, L., Widom, M., & Hawk, J. (2017). Thermodynamics of concentrated solid solution alloys. *Current Opinion in Solid State and Materials Science, 21*(5), 238–251.
67. Kaufmann, K., & Vecchio, K. S. (2020). Searching for high entropy alloys: A machine learning approach. *Acta Materialia, 198*, 178–222.
68. Lederer, Y., Toher, C., Vecchio, K. S., & Curtarolo, S. (2018). The search for high entropy alloys: A high-throughput ab-initio approach. *Acta Materialia, 159*, 364–383.
69. Li, Y., & Guo, W. (2019). Machine-learning model for predicting phase formations of high-entropy alloys. *Physical Review Materials, 3*(9), 095005.
70. Yao, H., Qiao, J., Gao, M., Hawk, J., Ma, S., Zhou, H., & Zhang, Y. (2016). NbTaV-(Ti, W) refractory high-entropy alloys: Experiments and modeling. *Materials Science and Engineering A, 674*, 203–211.
71. Todai, M., Nagase, T., Hori, T., Matsugaki, A., Sekita, A., & Nakano, T. (2017). Novel TiNbTaZrMo high-entropy alloys for metallic biomaterials. *Scripta Materialia, 129*, 65–68.

72. Yao, H., Qiao, J., Hawk, J., Zhou, H., Chen, M., & Gao, M. (2017). Mechanical properties of refractory high-entropy alloys: Experiments and modeling. *Journal of Alloys and Compounds, 696*, 1139–1150.
73. Zhou, Z., Zhou, Y., He, Q., Ding, Z., Li, F., & Yang, Y. (2019). Machine learning guided appraisal and exploration of phase design for high entropy alloys. *npj Computational Materials, 5*(1), 1–9.
74. Huang, W., Martin, P., & Zhuang, H. L. (2019). Machine-learning phase prediction of high-entropy alloys. *Acta Materialia, 169*, 225–236.
75. Zhang, Y., Wen, C., Wang, C., Antonov, S., Xue, D., Bai, Y., & Su, Y. (2020). Phase prediction in high entropy alloys with a rational selection of materials descriptors and machine learning models. *Acta Materialia, 185*, 528–539.
76. Sheng, G., & Liu, C. T. (2011). Phase stability in high entropy alloys: Formation of solid-solution phase or amorphous phase. *Progress in Natural Science: Materials International, 21*(6), 433–446.
77. Islam, N., Huang, W., & Zhuang, H. L. (2018). Machine learning for phase selection in multi-principal element alloys. *Computational Materials Science, 150*, 230–235.
78. Sato, J., Omori, T., Oikawa, K., Ohnuma, I., Kainuma, R., & Ishida, K. (2006). Cobalt-base high-temperature alloys. *Science, 312*(5770), 90–91.
79. Liu, P., Huang, H., Antonov, S., Wen, C., Xue, D., Chen, H., Li, L., Feng, Q., Omori, T., & Su, Y. (2020). Machine learning assisted design of γ'-strengthened Co-base superalloys with multi-performance optimization. *npj Computational Materials, 6*(1), 1–9.
80. Qi, J., Cheung, A. M., & Poon, S. J. (2019). High entropy alloys mined from binary phase diagrams. *Scientific Reports, 9*(1), 1–10.
81. Wen, C., Zhang, Y., Wang, C., Xue, D., Bai, Y., Antonov, S., Dai, L., Lookman, T., & Su, Y. (2019). Machine learning assisted design of high entropy alloys with desired property. *Acta Materialia, 170*, 109–117.
82. Chang, Y.-J., Jui, C.-Y., Lee, W.-J., & Yeh, A.-C. (2019). Prediction of the composition and hardness of high-entropy alloys by machine learning. *JOM, 71*(10), 3433–3442.
83. Menou, E., Tancret, F., Toda-Caraballo, I., Ramstein, G., Castany, P., Bertrand, E., Gautier, N., & Díaz-Del, P. E. J. R. (2018). Computational design of light and strong high entropy alloys (HEA): Obtainment of an extremely high specific solid solution hardening. *Scripta Materialia, 156*, 120–123.
84. Yang, F., Li, Z., Wang, Q., Jiang, B., Yan, B., Zhang, P., Xu, W., Dong, C., & Liaw, P. K. (2020). Cluster-formula-embedded machine learning for design of multicomponent β-Ti alloys with low Young's modulus. *npj Computational Materials, 6*(1), 1–11.
85. Roy, A., Babuska, T., Krick, B., & Balasubramanian, G. (2020). Machine learned feature identification for predicting phase and Young's modulus of low-, medium-and high-entropy alloys. *Scripta Materialia, 185*, 152–158.
86. Kim, G., Diao, H., Lee, C., Samaei, A., Phan, T., de Jong, M., An, K., Ma, D., Liaw, P. K., & Chen, W. (2019). First-principles and machine learning predictions of elasticity in severely lattice-distorted high-entropy alloys with experimental validation. *Acta Materialia, 181*, 124–138.
87. Huang, S., Tian, F., & Vitos, L. (2018). Elasticity of high-entropy alloys from ab initio theory. *Journal of Materials Research, 33*(19), 2938–2953.
88. Lee, C., Kim, G., Chou, Y., Musicó, B. L., Gao, M. C., An, K., Song, G., Chou, Y.-C., Keppens, V., & Chen, W. (2020). Temperature dependence of elastic and plastic deformation behavior of a refractory high-entropy alloy. *Science Advances, 6*(37), eaaz4748.
89. Dai, F.-Z., Wen, B., Sun, Y., Xiang, H., & Zhou, Y. (2020). Theoretical prediction on thermal and mechanical properties of high entropy (Zr0. 2Hf0. 2Ti0. 2Nb0. 2Ta0. 2) C by deep learning potential. *Journal of Materials Science and Technology, 43*, 168–174.